PHYSICAL REVIEW B **77**, 224441 (2008)

Magnetodielectric phenomena in a charge- and spin-frustrated system of layered iron oxide

Makoto Naka, Aya Nagano,* and Sumio Ishihara
Department of Physics, Tohoku University, Sendai 980-8578, Japan
(Received 3 March 2008; revised manuscript received 24 April 2008; published 27 June 2008)

Dielectric and magnetic phenomena in spin- and charge-frustrated system $R\mathrm{Fe_2O_4}$ (R is a rare-earth metal ion) are studied. An electronic model for charge, spin, and orbital degrees in a pair of triangular-lattice planes is derived. We analyze this model by utilizing the mean-field approximation and the Monte Carlo simulation in a finite size cluster. A threefold-type charge-ordered structure with charge imbalance between the planes is stabilized in finite temperatures. This polar charge order is reinforced by spin ordering of Fe ions. This magnetodielectric phenomenon is caused by spin frustration and charge-spin coupling in the exchange interaction. We show cross-correlation effect in magnetic- and electric-field responses. Oxygen-deficiency effect as an impurity effect in a frustrated charge-spin coupled system is also examined.

DOI: 10.1103/PhysRevB.77.224441 PACS number(s): 75.80.+q, 72.80.Ga, 75.10.−b, 77.80.−e

I. INTRODUCTION

The simultaneous existence of electric and magnetic polarizations and their control by external field have recently been revived as multiferroic phenomena in correlated electron oxides.[1–4] Behind the large coupling between electric and magnetic moments, spin frustration plays dominant roles on multiferroic properties. Noncollinear spin structures, such as cycloid, spiral, and so on, are realized in frustrated spin systems, and spontaneous electric polarization is induced to gain the symmetric and/or antisymmetric exchange interactions.[5–10] From this viewpoint, this class of materials is recognized as a spin driven ferroelectricity. Another class of ferroelectricity can be considered. Apart from the integer filling of electron in valence bands, a charge degree of freedom arises. The long-range charge order due to the Coulomb interaction is ubiquitously observed in several transition-metal compounds.[11–13] When electronic charge is ordered without inversion symmetry, a macroscopic electric polarization appears. In the case where this electric polarization can be reversed by external electric field, it is a ferroelectric state driven by electronic charge degree of freedom. Some low-dimensional organic salts, e.g., the neutral-ionic transition system[14,15] and α-$(\mathrm{BEDT\text{-}TTF})_2\mathrm{I}_3$,[16] are considered to belong to this class of ferroelectric materials. A charge polarized state observed in a layered structure manganite $\mathrm{Pr}(\mathrm{Sr}_{0.1}\mathrm{Ca}_{0.9})_2\mathrm{Mn_2O_7}$ is attributed to the charge order associated with orbital order and lattice distortion.[17] The possibility of ferroelectricty in charge-ordered manganites is also proposed from a theoretical viewpoint.[18]

Rare-earth iron oxides with layered crystal structure $R\mathrm{Fe_2O_4}$ (R=Lu, Y, Yb, and Er)[19] of the present interest belong to this class of ferroelectricity. The crystal structure of $R\mathrm{Fe_2O_4}$ consists of paired Fe-O triangular-lattice layers and R-O blocks stacked along the c axis. A schematic view of a paired Fe-O layer, termed the W layer, is shown in Fig. 1(a). The average valence of Fe ions is +2.5, which implies that equal amounts of Fe^{2+} and Fe^{3+} occupy the W layer. Charge structure was investigated by the electron and x-ray diffraction experiments.[20–22] In $\mathrm{LuFe_2O_4}$, below 500 K, streak-type diffuse scattering was observed along $(1/3\ 1/3\ l)$ lines, and below 320 K, spots appear at $(1/3\ 1/3\ 3m+1/2)$ in the streak lines associated with zigzag modulations. In this paper, we use the hexagonal index, although the space group is $R\bar{3}m$. These experimental results are interpreted as two- and three-dimensional charge orders of electrons. The three-dimensional order of Fe^{2+} and Fe^{3+} was also confirmed by the resonant x-ray scattering technique at Fe K edge.[23] As for the magnetic properties, magnetization in $\mathrm{LuFe_2O_4}$ starts to increase around 250 K.[24] Neutron diffraction experiments revealed that magnetic Bragg peaks at $(1/3\ 1/3\ m)$ appear and a ferrimagnetic order is realized below this temperature.[25–29] Electric polarization and dielectric anomalies were observed around the three-dimensional charge-ordering temperature, although the dielectric constant shows a strong dispersive and diffusive nature.[23,30] Several magnetodielectric phenomena were also reported around the ferrimagnetic ordering temperature.[23,31,32] It is worth noting that these dielectric and magnetic phenomena depend on the rare-earth metal element R and the oxygen stoichiometry; in $\mathrm{YFe_2O_4}$, with decreasing temperature, the threefold-type charge order is changed into a fourfold-type one, which is extremely sensitive to oxygen deficiency.[33–35]

To elucidate the mechanism of dielectric phenomena in $R\mathrm{Fe_2O_4}$, Yamada *et al.*[21] proposed a model for the threefold-type charge order. This charge-structure model is shown in Fig. 5(a), which will be introduced in more detail in Sec. III. This is a $\sqrt{3}\times\sqrt{3}$ structure in a plane, and along [110], electronic charges are aligned $\cdots\mathrm{Fe}^{3+}\mathrm{Fe}^{3+}\mathrm{Fe}^{2+}\cdots$ in the lower plane and $\cdots\mathrm{Fe}^{3+}\mathrm{Fe}^{2+}\mathrm{Fe}^{2+}\cdots$ in the upper one. That is, electronic charge is polarized between the upper and lower planes, and finite electric dipole moments exist in the W

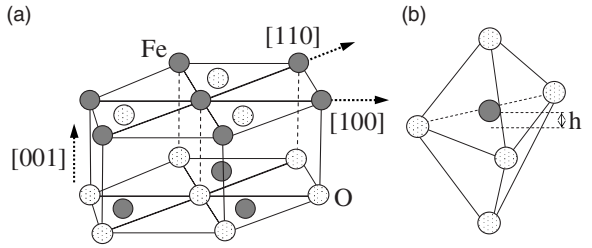

FIG. 1. (a) A pair of triangular-lattice planes (W layer). (b) A $\mathrm{FeO_5}$ cluster.

layer. Based on this polar charge model and the neutron diffraction data, a possible spin structure in the ferrimagnetic ordered phase was proposed.[34]

Through a number of the experimental results[19,21,23–25] and the theoretical analyses,[20,27,36–38] it is recognized that the electric polarization in this material is attributed to $3d$ electronic charge order. Besides, electronic charges strongly couple with spins, and charge and spin frustrations in the W layer play dominant roles in dielectric and magnetic properties. In this paper, we present a microscopic theory of electronic structure and magnetodielectric phenomena in $R\mathrm{Fe}_2\mathrm{O}_4$. We focus on $3d$ electronic structure in a W layer which is a minimum and main stage for the low-energy electronic state. We first suggest the orbital degree of freedom in a Fe^{2+} ion and derive an electronic Hamiltonian in a W layer. This model consists of the long-range Coulomb interactions and the exchange interaction derived from the generalized pd model. We analyze the charge structure by using the mean-field approximation and the Monte Carlo (MC) simulation. The threefold-type polar charge order competes with other type nonpolar ones and is stabilized at finite temperature. This is caused by charge fluctuation in a triangular lattice. We, furthermore, examine spin structure and coupling between spin ordering and electric polarization. The polar charge order is strongly stabilized below the magnetic ordering temperature. This magnetodielectric phenomenon is attributed to spin frustration in a triangular lattice. We demonstrate electric and magnetic responses that are available to examine the present theoretical scenario. The effects of oxygen deficiency on electric polarization are also studied.

In Sec. II, we derive the model Hamiltonian for electronic structure in a W layer. In Sec. III, numerical results for the charge structure and electric polarization are presented. Calculated results for the spin structure and the magnetodielectric responses are shown in Sec. IV. Examined oxygen-deficiency effects are introduced in Sec. V. Section VI is devoted to discussion and concluding remarks. Preliminary results for the present study have been published in Refs. 36 and 37. Study of a doubly degenerate orbital model in a honeycomb lattice as an orbital model for $R\mathrm{Fe}_2\mathrm{O}_4$ is presented in separate papers.[37,39]

II. MODEL HAMILTONIAN

We start from the electronic structure in a single Fe ion in the W layer. This ion is fivefold coordinate with three O ions in the xy plane and two at apices, as shown in Fig. 1(b). We calculate the crystalline-field splitting of the Fe $3d$ orbitals in the FeO_5 cluster which belongs to the point group D_{3d}. Five O ions are replaced by point charges with valence of $-2e$, and their positions are determined by the crystal structure data.[40,41] The hydrogenlike wave functions are adopted for the Fe $3d$ orbitals, and the effective nuclear charge is taken to be +8. The split $3d$ orbitals are identified by the irreducible representations of the D_{3d} point group that have a basis in the d manifold: the $d_{3z^2-r^2}$ orbital with A' and two sets of the doubly degenerate orbitals $(-ad_{zx}+bd_{x^2-y^2}, ad_{yz}+bd_{xy})$ with E' and $(ad_{x^2-y^2}+bd_{zx}, -ad_{xy}+bd_{yz})$ with E''. Numerical coefficients a and b satisfy the relation $a^2+b^2=1$. We obtain that the degenerate E' orbitals take the lowest energy with $b=0.89$, and the first excited level is E''. The energy difference between E' and E'', $\Delta E_{E'-E''}$, is about 0.1 eV, which is smaller than that between E'' and A', $\Delta E_{E''-A'} \sim 0.6$ eV. When we see the crystal structure in detail, an Fe ion is not located at the center of a O_5 cage. Distance between the Fe ion and the O_3 plane denoted by h [see Fig. 1(b)] is about 0.1 Å in $\mathrm{LuFe}_2\mathrm{O}_4$.[40,41] We obtain that, with taking h into account, $\Delta E_{\mathrm{E}'-\mathrm{E}''}$ increases and $\Delta E_{E''-A'}$ decreases. The hybridization effects between Fe $3d$ and O $2p$ orbitals may increase these level separations. However, because of the small value of $\Delta E_{E'-E''}$, we do not exclude a possibility that $(d_{x^2-y^2}, d_{xy})$ and (d_{zx}, d_{yz}) strongly couple with each other, i.e., $a \sim b$, and that the E'' level is the lowest. In any cases, the lowest orbitals are degenerate. As a result, in Fe^{3+}, each orbital is singly occupied, and total spin $S=5/2$ of the high-spin state. On the other hand, in Fe^{2+}, one of the degenerate lowest levels is doubly occupied by a hole, and $S=2$. Thus, twofold orbital degeneracy exists in Fe^{2+}. This is represented by the orbital pseudospin operator defined by

$$\mathbf{T}_i = \frac{1}{2} \sum_{\mu\mu' s} d^{\dagger}_{i\mu s} \sigma_{\mu\mu'} d_{i\mu' s}, \tag{1}$$

where $d^{\dagger}_{i\mu s}$ is the creation operator for an Fe $3d$ hole with orbital μ, spin $s(=\uparrow,\downarrow)$ at site i, and $\sigma_{\mu\mu'}$ are the Pauli matrices. In following part of this paper, we assume for simplicity that the two orbitals in the lowest level are $(d_{x^2-y^2}, d_{xy})$, and the index μ in Eq. (1) takes the values x^2-y^2 and xy. The z component of the operator T^z_i is $1/2$ $(-1/2)$ for the state where a hole occupies the $d_{x^2-y^2}$ (d_{xy}) orbital. Even in the case where the orbitals in the lowest level are (d_{zx}, d_{yz}), the following part of this paper is valid by reinterpreting that the index μ in Eq. (1) takes the values yz and zx.

We set up the model Hamiltonian for the electronic structure in a W layer. The $3d$ electrons in the Fe ions and the $2p$ ones in O which hybridizes with Fe $3d$ are introduced. We start from the following generalized pd Hamiltonian:

$$\mathcal{H}_{pd} = \mathcal{H}_d + \mathcal{H}_p + \mathcal{H}_t + \mathcal{H}_V, \tag{2}$$

with

$$\begin{aligned}\mathcal{H}_d = & \sum_{i\mu\sigma} \varepsilon^d_{\mu} d^{\dagger}_{i\mu\sigma} d_{i\mu\sigma} + \sum_{i\mu} U^d n^d_{i\mu\uparrow} n^d_{i\mu\downarrow} \\ & + \frac{1}{2} \sum_{i\mu\neq\mu'\sigma\sigma'} W^d n^d_{i\mu\sigma} n^d_{i\mu'\sigma'} \\ & - \frac{1}{2} \sum_{i\mu\neq\mu'\sigma\sigma'} I^d d^{\dagger}_{i\mu\sigma} d_{i\mu\sigma'} d^{\dagger}_{i\mu'\sigma'} d_{i\mu'\sigma},\end{aligned} \tag{3}$$

$$\begin{aligned}\mathcal{H}_p = & \sum_{j\nu\sigma} \varepsilon^p_{\nu} p^{\dagger}_{j\nu\sigma} p_{j\nu\sigma} + \sum_{j\nu} U^p n^p_{j\nu\uparrow} n^p_{j\nu\downarrow} \\ & + \frac{1}{2} \sum_{j\nu\neq\nu'\sigma\sigma'} W^p n^p_{j\nu\sigma} n^p_{j\nu'\sigma'} \\ & - \frac{1}{2} \sum_{j\nu\neq\nu'\sigma\sigma'} I^p p^{\dagger}_{j\nu\sigma} p_{j\nu\sigma'} p^{\dagger}_{j\nu'\sigma'} p_{j\nu'\sigma},\end{aligned} \tag{4}$$

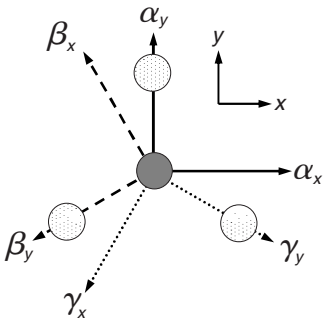

FIG. 2. Three two-dimensional coordinates (α_x, α_y), (β_x, β_y), and (γ_x, γ_y) in a FeO triangular lattice. Filled and dotted circles represent Fe and O ions, respectively.

$$\mathcal{H}_t = \sum_{i\eta\sigma} t^{pd} d^{\dagger}_{i\eta_x^2-\eta_y^2\sigma} p_{i+\delta_\eta \eta_y \sigma} + \text{H.c.}, \tag{5}$$

$$\mathcal{H}_V = \left(\sum_{\langle ij \rangle}^{ab\text{NN}} V_{ab\text{NN}} + \sum_{\langle ij \rangle}^{c\text{NN}} V_{c\text{NN}} + \sum_{\langle ij \rangle}^{c\text{NNN}} V_{c\text{NNN}} \right) n_i^d n_j^d, \tag{6}$$

where $d^{\dagger}_{i\mu\sigma}$ is the creation operator for the Fe $3d$ hole with orbital μ $(=xy, x^2-y^2, yz, zx, 3z^2-r^2)$ and spin σ $(=\uparrow, \downarrow)$ at site i and $p^{\dagger}_{j\nu\sigma}$ is for the O $2p$ hole with orbital ν $(=x, y, z)$. Number operators are defined by $n^d_{i\mu\sigma} = d^{\dagger}_{i\mu\sigma} d_{i\mu\sigma}$, $n^p_{j\nu\sigma} = p^{\dagger}_{j\nu\sigma} p_{j\nu\sigma}$, and $n^d_i = \Sigma_{\mu\sigma} n^d_{i\mu\sigma}$. A symbol δ_η is a connecting vector between Fe and nearest neighboring (NN) O ions along direction η. Interactions in a Fe ion are described in the first term of Eq. (2), $\mathcal{H}_d$, where the level energy ε^d_μ, the intraorbital Coulomb interaction U^d, the interorbital one W^d, and the exchange interaction I^d are considered. Interactions in $\mathcal{H}_p$ are defined in the same way with those in $\mathcal{H}_d$. Hopping of a hole between the NN Fe and O ions in the same plane is described in $\mathcal{H}_t$ with the transfer integral t^{pd}. For convenience, we introduce the three two-dimensional coordinates (η_x, η_y), with $\eta = (\alpha, \beta, \gamma)$, which are obtained by a rotation of the xy axis by $2\pi m_\eta/3$, with $(m_\alpha, m_\beta, m_\gamma) = (0, 1, 2)$ (see Fig. 2). In each coordinate, we define the operators as

$$\begin{pmatrix} d_{i\eta_x^2-\eta_y^2\sigma} \\ d_{i\eta_x\eta_y\sigma} \end{pmatrix} = \begin{pmatrix} \cos\frac{4\pi}{3} m_\eta & \sin\frac{4\pi}{3} m_\eta \\ -\sin\frac{4\pi}{3} m_\eta & \cos\frac{4\pi}{3} m_\eta \end{pmatrix} \begin{pmatrix} d_{ix^2-y^2\sigma} \\ d_{ixy\sigma} \end{pmatrix} \tag{7}$$

and

$$\begin{pmatrix} p_{i\eta_x\sigma} \\ p_{i\eta_y\sigma} \end{pmatrix} = \begin{pmatrix} \cos\frac{2\pi}{3} m_\eta & \sin\frac{2\pi}{3} m_\eta \\ -\sin\frac{2\pi}{3} m_\eta & \cos\frac{2\pi}{3} m_\eta \end{pmatrix} \begin{pmatrix} p_{ix\sigma} \\ p_{iy\sigma} \end{pmatrix}. \tag{8}$$

In the bond direction η, the $d_{\eta_x^2-\eta_y^2}$ and p_{η_y} orbitals compose the σ bond. The intersite Coulomb interactions between Fe ions are taken into account in the last term of Eq. (2), i.e., $\mathcal{H}_V$. We consider the largest three interactions in the W layer, as shown in Fig. 3: the interplane NN interaction ($V_{c\text{NN}}$), the intraplane NN one ($V_{ab\text{NN}}$), and the interplane next NN one ($V_{c\text{NNN}}$). This is because (1) these Coulomb interactions are a minimum set that reproduces the three types of charge structures experimentally observed, and (2) a distance between the fourth neighbor Fe ions in the W layer is comparable to that between the NN W layers. This will be discussed in Sec. III in more detail. Summations in $\mathcal{H}_V$ take the three kinds of pairs. When the $1/r$-type Coulomb interaction is assumed, we obtain $V_{c\text{NN}}/V_{ab\text{NN}} = 1.2$ and $V_{c\text{NNN}}/V_{ab\text{NN}} = 0.77$ for $LuFe_2O_4$. By introducing the pseudospin operator Q^z_i for charge degree of freedom, $\mathcal{H}_V$ is rewritten as an antiferromagnetic Ising model,

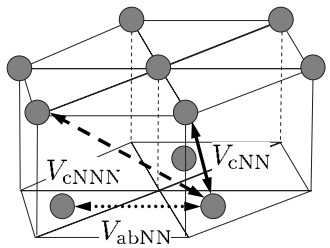

FIG. 3. Intersite Coulomb interactions between Fe ions. The solid, broken, and dotted arrows represent interactions between the nearest neighbor ($V_{c\text{NN}}$), the next nearest neighbor ($V_{ab\text{NN}}$), and the third neighbor ($V_{c\text{NNN}}$) Fe-Fe bonds, respectively.

$$\mathcal{H}_V = \left(\sum_{\langle ij \rangle}^{c\text{NN}} V_{c\text{NN}} + \sum_{\langle ij \rangle}^{ab\text{NN}} V_{ab\text{NN}} + \sum_{\langle ij \rangle}^{c\text{NNN}} V_{c\text{NNN}} \right) Q^z_i Q^z_j, \tag{9}$$

where a constant term is omitted. The operator Q^z_i takes $1/2$ and $-1/2$ for Fe^{3+} and Fe^{2+}, respectively. The charge conservation is imposed by a relation $\Sigma_i Q^z_i = 0$.

Based on the extended pd Hamiltonian $\mathcal{H}_{pd}$, we derive the effective Hamiltonian for the superexchange interactions between NN Fe ions in a plane. This interaction arises from virtual hopping of holes between Fe ions. The Hamiltonian is derived by the fourth order projection-perturbation procedure in terms of the hopping term $\mathcal{H}_{pd}$. The following two exchange processes are considered:

$$d^M p^0 d^N \rightarrow d^{M+1} p^0 d^{N-1} \rightarrow d^M p^0 d^N, \tag{10}$$

and

$$d^M p^0 d^N \rightarrow d^{M-1} p^2 d^{N-1} \rightarrow d^M p^0 d^N, \tag{11}$$

where we adopt the hole picture, and M and N represent the numbers of holes. These are termed the dd and dpd processes, respectively, from now on. Here, we present the outline of derivation, and details are given in Appendix A. A general form of the Hamiltonian is

$$\mathcal{H}_J = \hat{P}\mathcal{H}_t \frac{1}{E_i - \mathcal{H}_0} \hat{Q}\mathcal{H}_t \frac{1}{E_i - \mathcal{H}_0} \hat{Q}\mathcal{H}_t \frac{1}{E_i - \mathcal{H}_0} \hat{Q}\mathcal{H}_t \hat{P}, \tag{12}$$

where $\hat{P}$ is the projection operator for the d^5 (d^4) high-spin states in Fe^{3+} (Fe^{2+}), $\hat{Q} = 1 - \hat{P}$ and E_i is the initial-state energy. Many body effects of $\mathcal{H}_V$ in the intermediate states are considered approximately; we assume that the intermediate-state energies for $d^{M+1} p^0 d^{N-1}$ [see Eq. (10)] are higher than the initial- and final-state energies by a constant energy parameter $\hat{V}$, which is of the order of the intersite Coulomb

interaction. Then, we set $\mathcal{H}_0=\mathcal{H}_d+\mathcal{H}_p+\hat{V}$. We interpret that effects of $\mathcal{H}_V$ in other intermediate states are included in the charge-transfer energy, Δ_{CT}, between the $d_{\eta_x^2-\eta_y^2}$ and p_{η_y} orbitals. The obtained Hamiltonian $\mathcal{H}_J$ is classified by valences of Fe ions in the initial states, i.e., Fe^{m+}-Fe^{n+} where n and m take 2 and 3, and electron configurations in the intermediate states denoted by k. The Hamiltonian is given as

$$\mathcal{H}_J=\sum_{(mn)k}\mathcal{H}^{(mn)-k}. \tag{13}$$

All possible intermediate states k are taken into account in Eq. (13) which consists of six terms in $\mathcal{H}^{(22)-k}$ and $\mathcal{H}^{(23)-k}$ and four terms in $\mathcal{H}^{(33)-k}$. Explicit formulas of all terms are presented in Appendix A. Here, we show some representative terms:

$$\mathcal{H}^{(22)-1}=J^{(22)-1}\sum_{\langle ij\rangle}(\mathbf{I}_i\cdot\mathbf{I}_j+6)\left(\frac{1}{2}-2\tau_{i\eta_i}\tau_{j\eta_j}\right)\times\left(\frac{1}{2}-Q_i^z\right)\left(\frac{1}{2}-Q_j^z\right), \tag{14}$$

$$\mathcal{H}^{(23)-1}=J^{(23)-1}\sum_{\langle ij\rangle}\left(\mathbf{J}_i\cdot\mathbf{I}_j+\frac{15}{2}\right)\left(\frac{1}{2}-\tau_{j\eta_j}\right)\times\left(\frac{1}{2}+Q_i^z\right)\left(\frac{1}{2}-Q_j^z\right), \tag{15}$$

$$\mathcal{H}^{(33)-1}=J^{(33)-1}\sum_{\langle ij\rangle}\left(\mathbf{J}_i\cdot\mathbf{J}_j-\frac{25}{4}\right)\left(\frac{1}{2}+Q_i^z\right)\left(\frac{1}{2}+Q_j^z\right). \tag{16}$$

We define the spin operators $\mathbf{I}_i$ and $\mathbf{J}_i$ for Fe^{2+} and Fe^{3+} with amplitudes of 2 and 5/2, respectively. The orbital operator is redefined in the (η_x,η_y) coordinate as

$$\tau_{i\eta}=T_i^z\cos\left(\frac{2\pi}{3}m_\eta\right)+T_i^x\sin\left(\frac{2\pi}{3}m_\eta\right). \tag{17}$$

This operator takes 1/2 (−1/2), when the $d_{\eta_x^2-\eta_y^2}$ ($d_{\eta_x\eta_y}$) orbital is occupied by a hole. In a given pair of i and j sites, subscripts η_i and η_j in $\tau_{i\eta_i}$ and $\tau_{j\eta_j}$ are automatically determined. The exchange constants are defined by $J^{(22)-1}=-t_{ddc}^2/[10\Delta_{(22)-1}]$, $J^{(23)-1}=-2t_{ddc}^2/[25\Delta_{(23)-1}]$, and $J^{(33)-1}=4t_{ddc}^2/[25\Delta_{(33)-1}]$, where t_{ddc} is the transfer integral between NN Fe ions defined by $t_{ddc}=(t_{pd}^2\cos\theta)/\Delta_{\mathrm{CT}}$ with the Fe-O-Fe bond angle θ (=120°). We introduce the intermediate-state energies as $\Delta_{(22)-1}=W^d-I^d+\hat{V}$, $\Delta_{(23)-1}=\hat{V}$, and $\Delta_{(33)-1}=U^d+4I^d+\hat{V}$. It is worth noting that (1) $\mathcal{H}^{(22)-l}$ is expressed as a product of charge, spin, and orbital interactions between given sites i and j, and (2) $\mathcal{H}^{(32)-l}$ includes a linear term of the orbital pseudospin because Fe^{3+} does not have the orbital degree of freedom.

After all, we obtain the Coulomb- and exchange-interaction Hamiltonian

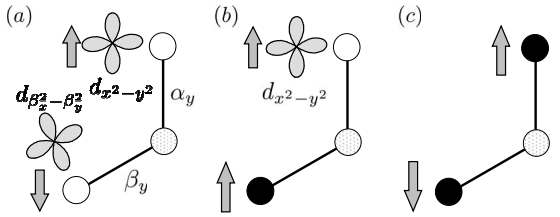

FIG. 4. The lowest-energy spin and orbital configurations (a) for Fe^{2+}-Fe^{2+} bond, (b) for Fe^{3+}-Fe^{2+}, and (c) for Fe^{3+}-Fe^{3+}. The open, filled, and dotted circles represent Fe^{2+}, Fe^{3+}, and O ions, respectively. Spin and orbital configuration in (a) is energetically close to ferromagnetic spin alignment with $d_{x^2-y^2}$ and $d_{\beta_x\beta_y}$ orbitals.

$$\mathcal{H}=\mathcal{H}_V+\mathcal{H}_J, \tag{18}$$

where $\mathcal{H}_V$ and $\mathcal{H}_J$ are given in Eqs. (9) and (13), respectively. Before going to the numerical results calculated in the Hamiltonian, we briefly mention the energy scales of charge, spin, and orbital degrees of freedom and signs of the exchange interactions. The intersite Coulomb interactions provide a larger energy scale than the exchange interactions. Thus, the charge sector is frozen at the highest temperature in comparison with spin and orbital ones. This is consistent with the experimental results in $LuFe_2O_4$ where the charge-ordering temperature (about 320 K) is higher than the spin ordering one (about 250 K).[20,21,27] By calculating the exchange energy in a given NN bond, we estimate stable spin and orbital configurations. This is not trivial from the Goodenough–Kanamori rule because of the 120° bond angle. The energy parameter sets for the exchange coupling constant $J^{(mn)-l}$ are determined from the experimental data in $LaFeO_3$,[42,43] and $\mathbf{I}_i$ and $\mathbf{J}_i$ are assumed to be the Ising spins. We obtain the spin and orbital configurations for the lowest exchange energies as (1) for a Fe^{2+}-Fe^{2+} bond, $I_i^zI_j^z=-4$ (antiferromagnetic) and $\tau_i=\tau_j=1/2$, which is energetically close to $I_i^zI_j^z=4$ (ferromagnetic) and $\tau_i=-\tau_j=1/2$, (2) for Fe^{3+}-Fe^{3+}, $J_i^zJ_j^z=-25/4$ (antiferromagnetic), and (3) for Fe^{2+}-Fe^{3+}, $I_i^zJ_j^z=5$ (ferromagnetic) and $\tau_i=1/2$. The schematic views for the stable configurations are presented in Fig. 4. In the neutron scattering experiments, the ferrimagnetic phase indexed as $(1/3\ 1/3\ m)$ appears around 250 K. Possible magnetic structures are shown in Fig. 13, which will be explained in more detail later. In this structure, Fe^{2+} ions in the $2\mathrm{Fe}^{3+}$-Fe^{2+} (upper) plane are surrounded by six NN Fe^{3+}. Thus, the exchange Hamiltonian in this plane is reduced into a form of $\Sigma_{\langle ij\rangle}[(1/2)\pm\tau_{i\eta_i}]$ which becomes a constant by using the relation of $\Sigma_{\langle ij\rangle}\tau_{i\eta_i}=0$. This relation is also applicable to the Fe^{2+}-Fe^{3+} bonds in the $2\mathrm{Fe}^{2+}$-Fe^{3+} (lower) plane where three Fe^{2+}-Fe^{3+} bonds connecting a Fe^{2+} ion are equivalent [see Fig. 13]. Therefore, the orbital part of the exchange Hamiltonian in this ferrimagnetic phase is mapped onto the following orbital model defined on a Fe^{2+} sublattice:

$$\mathcal{H}_{\mathrm{orb}}=J_{\mathrm{orb}}\sum_i{}'(\tau_{i\beta}\tau_{i+\mathbf{e}_\alpha\gamma}+\tau_{i\gamma}\tau_{i+\mathbf{e}_\beta\alpha}+\tau_{i\alpha}\tau_{i+\mathbf{e}_\gamma\beta}), \tag{19}$$

where $(\mathbf{e}_\alpha,\mathbf{e}_\beta,\mathbf{e}_\gamma)$ represent the three unit vectors connecting NN Fe^{2+} sites in a honeycomb lattice. A summation Σ_i' takes

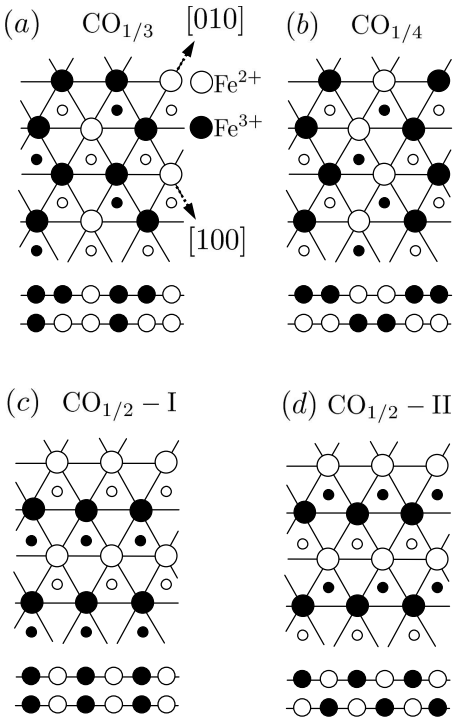

FIG. 5. Charge structures in a W layer: (a) $CO_{1/3}$, (b) $CO_{1/4}$, (c) $CO_{1/2}-I$, and (d) $CO_{1/2}-II$. The filled and open circles represent Fe^{3+} and Fe^{2+}, respectively, and large and small circles are for Fe ions in the upper and lower planes, respectively. Lower panel in each figure is a side view from $[1\bar{1}0]$.

Fe^{2+} sites in one of the two sublattices in a honeycomb lattice. The coupling constant $J_{\rm orb}$ is given by the exchange constants $J^{(nm)-k}$. In this model, it is theoretically obtained that the orbital does not show a conventional long-range order down to very low temperature of the order of $0.005J_{\rm orb}$. Therefore, for simplicity, we assume that the pseudospin operators for orbital in $\mathcal{H}_J$ are set to be zero in the following calculation. Theoretical study of the orbital model on a honeycomb lattice is presented in separate papers.[37,39]

III. CHARGE STRUCTURE AND ELECTRIC POLARIZATION

First, we focus on the charge structure and the electric polarization by analyzing the intersite Coulomb interaction term $\mathcal{H}_V$. We apply, at the first stage, the mean-field approximation to $\mathcal{H}_V$ and obtain stable charge structures. The charge conservation is taken into account by adding the chemical potential term, $-V_{\rm ext}\Sigma_i Q_i^z$, in the Hamiltonian. We assume that the expectation value $\langle Q_i^z\rangle$ is periodic along the $\langle 110\rangle$ or $\langle 210\rangle$ directions and takes the same amplitude along $\langle \bar{1}10\rangle$ or $\langle 010\rangle$, respectively. Periodicity L is taken up to 12. In upper and lower planes, $\langle Q_i^z\rangle$'s are independent and have the same periodicity along the $\langle 110\rangle$ or $\langle 210\rangle$ directions. Each solution is characterized by the momentum $\mathbf{q}\equiv(M/2L,M/2L,n)$ or $(M/2L,0,n)$, where M is the number of nodes of $\langle Q_i^z\rangle$ along the $\langle 110\rangle$ or $\langle 210\rangle$ directions, respectively. When a phase difference between $\langle Q_i^z\rangle$'s in the upper and lower planes is 0 (π), n takes 0 (1/2). Phase diagram is determined by comparing the free energy. Representative charge structures are shown in Fig. 5. Four types of CO's in Fig. 5, denoted by $CO_{1/3}$, $CO_{1/4}$, $CO_{1/2}-I$, and $CO_{1/2}-II$, are characterized by momenta $\mathbf{q}=(1/3,1/3,0)\equiv\mathbf{q}_{1/3}$, $(1/4,1/4,1/2)\equiv\mathbf{q}_{1/4}$, $(1/2,1/2,0)\equiv\mathbf{q}_{1/2-I}$, and $(1/2,0,0)\equiv\mathbf{q}_{1/2-II}$, respectively. As suggested by Yamada *et al.*,[20,21] $CO_{1/3}$ shows finite electric polarization due to charge imbalance between the two triangular-lattice planes. A ratio of Fe^{2+} and Fe^{3+} is 1:2 (2:1) in the upper (lower) plane. In other charge structures, equal numbers of Fe^{2+} and Fe^{3+} occupy the upper and lower planes, and there is no electric polarization.

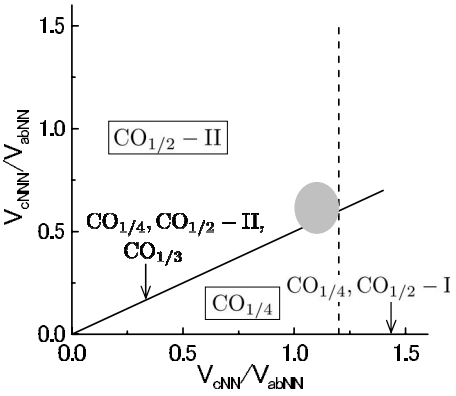

FIG. 6. Mean-field phase diagram for charge order at zero temperature. Three charge structures, $CO_{1/4}$, $CO_{1/2}-II$, and $CO_{1/3}$, are degenerate on a line of $V_{c\rm NN}=2V_{c\rm NNN}$ and the two, $CO_{1/4}$ and $CO_{1/2}-I$, are degenerate on a line of $V_{c\rm NNN}=0$. The shaded area corresponds to a region for $R\mathrm{Fe_2O_4}$. Phase diagram in finite temperatures, shown in Fig. 7, is calculated on broken line.

Mean-field phase diagram at zero temperature is presented in Fig. 6. The nonpolar $CO_{1/2}-II$ and $CO_{1/4}$ structures are stable in the regions of $V_{\rm CNN}/V_{\rm CNNN}<2$ and $V_{\rm CNN}/V_{\rm CNNN}>2$, respectively. The polar $CO_{1/3}$ structure appears only on the phase boundary where $CO_{1/3}$ is degenerate with $CO_{1/2}-II$ and $CO_{1/4}$. Realistic parameter values for $R\mathrm{Fe_2O_4}$ correspond to a shaded area in Fig. 6. We fix a value of $V_{c\rm NN}/V_{ab\rm NN}$ to be 1.2, as shown by a dashed line in Fig. 6, and calculate finite-temperature phase diagram (Fig. 7). The polar $CO_{1/3}$ is stabilized in a wide region between $CO_{1/4}$ and the $CO_{1/2}-II$.

Beyond the mean-field calculation, we examine the charge structure in finite temperature by using the MC simu-

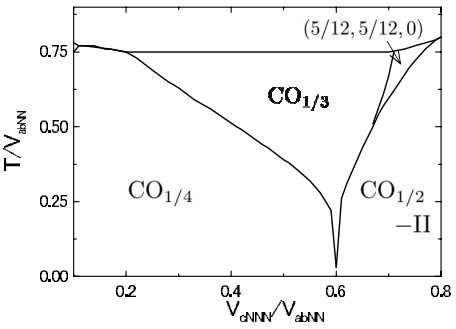

FIG. 7. Mean-field phase diagram for charge structure in finite temperatures. The Coulomb interaction $V_{c\rm NN}/V_{ab\rm NN}$ is chosen to be 1.2.

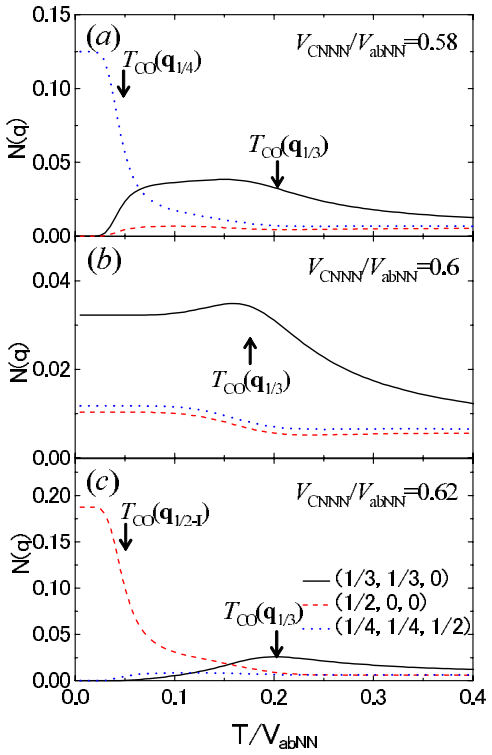

FIG. 8. (Color online) Charge correlation functions $N(\mathbf{q})$ at (a) V_{cNNN}/V_{abNN}=0.60, (b) 0.58, and (c) 0.62 calculated in $\mathcal{H}_V$. The Coulomb interaction V_{cNN}/V_{abNN} is chosen to be 1.2.

lation. To avoid a trap of a simulation in local minima, we adopt the multicanonical Monte Carlo (MUMC) method.[44] Simulations are performed on a paired triangular lattice of $L\times L\times 2(\equiv 2N)$ (L=6 and 12) sites with the periodic-boundary condition in the ab plane. We use 6×10^6 MC steps to obtain a histogram in the MUMC method and 16×10^6 MC steps for measurement. We calculate the charge correlation function and the electric polarization P defined by

$$N(\mathbf{q}) = \frac{1}{(2N)^2}\sum_{ij}\langle Q_i^z Q_j^z\rangle e^{-i\mathbf{q}\cdot(\mathbf{r}_i-\mathbf{r}_j)}, \tag{20}$$

$$P = \langle p^2\rangle^{1/2}, \tag{21}$$

with

$$p = \frac{1}{N}\left(\sum_i^u - \sum_i^l\right)Q_i^z, \tag{22}$$

where r_i is a position of site i and $\Sigma_i^{u(l)}$ represents a summation of site i in the upper (lower) plane.

The charge correlation functions at V_{cNNN}/V_{abNN}=0.58, 0.6, and 0.62 are presented in Fig. 8. At V_{cNNN}/V_{abNN}=0.6, $N(\mathbf{q}_{1/3})$ shows a hump around $\tilde{T}\equiv T/V_{abNN}$=0.18 and keeps a finite value down to the low temperature limit. From the specific heat data, we identify that $\tilde{T}$=0.18 corresponds to the charge-ordering temperature. In both cases of V_{cNNN}/V_{abNN} =0.58 and 0.62, $N(\mathbf{q}_{1/3})$ is dominant in high temperatures,

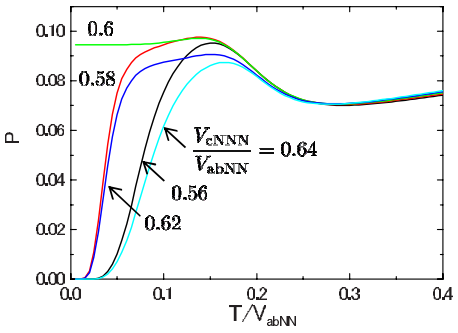

FIG. 9. (Color online) Electric polarization P as a functions of V_{cNNN}/V_{abNN} calculated in $\mathcal{H}_V$. The Coulomb interaction V_{cNN}/V_{abNN} is chosen to be 1.2.

starts to decrease around $\tilde{T}$=0.2, and disappears at the lowest temperature. On the contrary, the charge correlation $N(\mathbf{q}_{1/2-\text{II}})$ and $N(\mathbf{q}_{1/4})$ grow up around $\tilde{T}$=0.05 and increase with decreasing temperature. These results and the specific heat data imply that the charge order at $\mathbf{q}_{1/3}$ is changed into the other type of charge order at $\mathbf{q}_{1/4}$ ($\mathbf{q}_{1/2-\text{I}}$) around $\tilde{T}$ =0.04 (0.045) for V_{cNNN}/V_{abNN}=0.58 (0.62). Temperature dependence of P at several values of V_{cNNN}/V_{abNN} is presented in Fig. 9. At V_{cNNN}/V_{abNN}=0.6, P remains down to the low temperature limit. Apart from V_{cNNN}/V_{abNN}=0.6, P starts to decrease at the temperature where $N(\mathbf{q}_{1/2-\text{II}})$ and $N(\mathbf{q}_{1/4})$ grow up and disappears at the lowest temperature. These results obtained by the MUMC method are qualitatively consistent with the ones in the mean-field calculation.

The polar charge structure characterized by $\mathbf{q}_{1/3}$ and the transition to the another structure characterized by $\mathbf{q}_{1/4}$ at $V_{cNNN}/V_{abNN}<0.6$ are consistent with the experimental results. In $LuFe_2O_4$, charge order indexed as $(1/3\ 1/3\ 3m+1/2)$ appears around 350 K and remains, at least, down to around 20 K.[20] On the other hand, in YFe_2O_4, charge order indexed as $(1/3\ 1/3\ 3m+1/2)$ observed at room temperature is changed into the one as (1/4 1/4 3/4) around 250 K.[34,35] We suppose that different rare-earth metal ions slightly change ratio of the Coulomb potentials, and $LuFe_2O_4$ (YFe_2O_4) corresponds to the parameter region of $V_{cNNN}/V_{abNN}\approx 0.6$ ($V_{cNNN}/V_{abNN}<0.6$) in the present calculation.

Stability of the $CO_{1/3}$ phase is attributed to large thermal fluctuation in a triangular lattice. A key issue is the two-sublattice structure in this charge-ordered phase (see Fig. 10):[45] Fe^{2+} ions in the $2Fe^{2+}$-Fe^{3+} (lower) plane and Fe^{3+} in the Fe^{2+}-$2Fe^{3+}$ (upper) one belong to a sublattice termed A. Other Fe ions belong to another sublattice termed B. All in-plane NN ions of a site in the sublattice B have an opposite valence. On the other hand, a site on the sublattice A is surrounded by three NN Fe^{2+} and three NN Fe^{3+} in the plane. Therefore, the Coulomb potentials at these sites from the in-plane NN ions are canceled out, and charge fluctuation is able to easily occur without loss of V_{abNN}. It is obtained in the numerical calculation that an amplitude of the mean-field on the sublattice A is $0.9V_{abNN}$ at low temperature which is much less than that on the sublattice B, $2.1V_{abNN}$. Large charge fluctuation at the sites grows up with increasing tem-

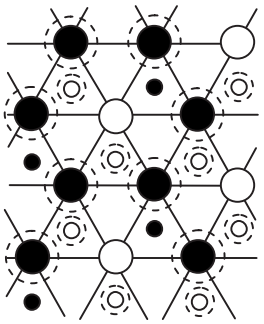

FIG. 10. Two-sublattice structure in the $CO_{1/3}$ phase. The amplitude of the mean field at Fe sites surrounded by broken circles is $0.9V_{abNN}$ and that at other sites is $2.1V_{abNN}$.

perature and contributes to the entropy gain at finite temperature. On the contrary, in the $CO_{1/2}-II$ and $CO_{1/4}$ structures, all Fe^{2+} (Fe^{3+}) are equivalent and charge fluctuation is weaker than that in the sublattice A of $CO_{1/3}$. This is the reason why the polar charge order characterized by (1/3, 1/3, 0) is more stable than other charge structures in finite temperatures.

Let us focus on the charge structure in low temperatures in more detail. As shown in Figs. 8(b) and 9, saturated values of $N(\mathbf{q}_{1/3})$ and P in $V_{cNNN}/V_{abNN}=0.6$ at the low temperature limit are 0.032 and 0.094, respectively, which are smaller than the values expected from the ideal $CO_{1/3}$ phase, 0.056 and 0.33 respectively. This implies that the charge configuration at low temperature in $V_{cNNN}/V_{abNN}=0.6$ is not the ideal $CO_{1/3}$ state. We analyze the probability histogram in the MUMC simulation and examine the charge configurations realized in the lowest temperatures. These are classified into the following three configurations: the polar $CO_{1/3}$ structure shown in Fig. 5(a), partially polarized charge structures characterized by the momentum $\mathbf{q}_{1/3}$, termed CO_A, and nonpolar structures termed CO_B. Detailed structures of CO_A and CO_B are shown in Appendix B. In CO_A, the polarization is $P=N/3-n\sqrt{N}$ with an integer number n satisfying a relation of $0\leq n\leq 2\sqrt{N}/3$. Degeneracy of a sum of these configurations is of the order of $\Sigma_{n2\sqrt{N}/3}C_n\sim 2^{\sqrt{N}}$ where ${}_kC_p=k!/[p!(k-p)!]$. As for the CO_B state, degeneracy of the configuration is also of the order of $2^{\sqrt{N}}$. Because of the coexistence of these charge structures, the saturated values of P and $N(\mathbf{q}_{1/3})$ are smaller than the expected values from the ideal $CO_{1/3}$ state. This tendency is remarkable in the large system size.

This coexistence of the polar and nonpolar CO states implies that the full polarization expected from the ideal $CO_{1/3}$ state is realized by additional weak interactions. The long-range Coulomb interactions between the NN W layers are one of the candidates. This scenario is plausible, since, in $LuFe_2O_4$, the electric polarization appears around the three-dimensional charge-ordering temperature.[23,30] We examine the effects of the inter-W-layer Coulomb interaction based on a model where two W layers stacked along the c axis are coupled by the Coulomb interaction. Saturated values of $N(\mathbf{q}_{1/3})$ and P at low temperature are identical to the expected values from the ideal polar $CO_{1/3}$ state. Roles of the exchange interaction as another candidate to lift the degeneracy are examined in Sec. IV.

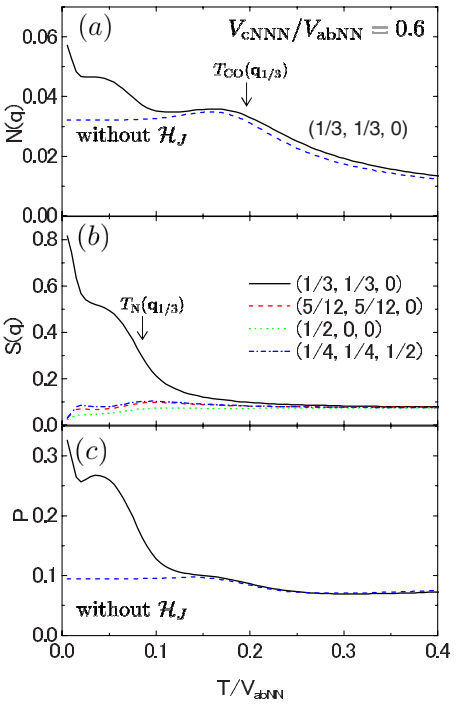

FIG. 11. (Color online) (a) Charge correlation functions $N(\mathbf{q})$, (b) spin correlation functions $S(\mathbf{q})$, and (c) electric polarization P calculated in $\mathcal{H}_V+\mathcal{H}_J$. The dashed lines in (a) and (c) are results obtained in $\mathcal{H}_V$. The parameters are chosen to be $V_{cNNN}/V_{abNN}=1.2$ and $V_{cNNN}/V_{abNN}=0.60$.

IV. SPIN STRUCTURE AND MAGNETOELECTRIC EFFECT

In this section, we introduce spin degree of freedom and examine coupling between the electric polarization and the magnetic ordering. The Hamiltonian $\mathcal{H}_V+\mathcal{H}_J$ is analyzed by utilizing the MUMC method in a $6\times6\times2$-site cluster. The spin operators $\mathbf{I}_i$ and $\mathbf{J}_i$ in $\mathcal{H}_J$ are assumed to be the Ising spins because of the strong magnetic anisotropy observed in RFe_2O_4.[27] The energy parameters in the Hamiltonian are chosen to be $U^d=7.8$, $W^d=6.2$, $I^d=0.8$, $U^p=4.1$, $W^p=2.9$, $I^p=0.6$, $t^{pd}=1.8$, $\Delta_{CT}=3$, and $\hat{V}=1$ in a unit of V_{abNN}. These are determined from the experimental data in $LaFeO_3$.[42,43] In this section, the orbital pseudospin operators in $\mathcal{H}_J$ are set to be zero, as explained in Sec. II. In particular, we focus on a parameter region around $V_{cNNN}/V_{abNN}=0.6$, where $CO_{1/3}$ is seen down to the lowest temperature in Fig. 7, and that around 0.58–0.59, where the transition from $CO_{1/3}$ to $CO_{1/4}$ is shown in Fig. 7.

Temperature dependences of the charge correlation function, the spin correlation function defined by

$$S(\mathbf{q})=\frac{1}{(2N)^2}\sum_{ij}\langle K_i^z K_j^z\rangle e^{-i\mathbf{q}\cdot(\mathbf{r}_i-\mathbf{r}_j)}, \tag{23}$$

where $K_i^z=I_i^z$ (J_i^z) for Fe^{2+} (Fe^{3+}) and the electric polarization are calculated. The results at $V_{cNNN}/V_{abNN}=0.60$ and 0.59 are shown in Figs. 11 and 12, respectively. For comparison, we also plot the data obtained in $\mathcal{H}_V$. At $V_{cNNN}/V_{abNN}=0.6$, three characteristic temperatures, $\tilde{T}=0.2$, 0.085, and 0.015,

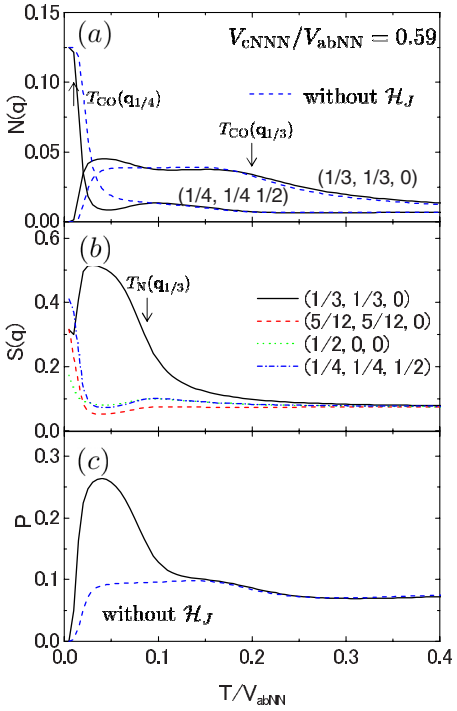

FIG. 12. (Color online) (a) Charge correlation functions $N(\mathbf{q})$, (b) spin correlation functions $S(\mathbf{q})$, and (c) electric polarization P calculated in $\mathcal{H}_V+\mathcal{H}_J$. The dashed lines in (a) and (c) are results obtained in $\mathcal{H}_V$. Parameters are chosen to be $V_{cNN}/V_{abNN}=1.2$ and $V_{cNNN}/V_{abNN}=0.59$.

are seen in $N(\mathbf{q}_{1/3})$. The highest one, $0.2[\equiv T_{CO}(\mathbf{q}_{1/3})]$, corresponds to the charge-ordering temperature for $CO_{1/3}$. Other two are the magnetic ordering ones at momentum $\mathbf{q}_{1/3}$. At $\tilde{T}=0.085[\equiv T_N(\mathbf{q}_{1/3})]$ and 0.015, spins in the Fe^{2+}-$2Fe^{3+}$ and $2Fe^{2+}$-Fe^{3+} planes in $CO_{1/3}$ (see Fig. 5) start to order, respectively. This double-magnetic transition may be an artifact in the present model where the interplane exchange interactions are neglected, and spins in the upper and lower planes are independent with each other. We expect that the interplane exchange interactions are much smaller than the in-plane ones. This is because, when electrons in the d_{xy} and $d_{x^2-y^2}$ orbitals are concerned, there are no exchange paths between Fe ions in an interplane NN bond. When higher-order exchange processes and/or contributions from other d orbitals are taken into account, weak interplane interactions may unify the double transition in the present calculation. As shown in Fig. 11, the charge correlation function at $\mathbf{q}_{1/3}$ and the polarization increase at $\tilde{T}=0.085$ and 0.014. Results clearly show that magnetic ordering enhances stability of the polar $CO_{1/3}$ phase. In the low temperature limit, $N(\mathbf{q}_{1/3})$ and P take 0.056 and 0.33, respectively, which are the ideal values in $CO_{1/3}$. At $V_{cNNN}/V_{abNN}=0.59$ (Fig. 12), a weak shoulder in $N(\mathbf{q}_{1/3})$ around $\tilde{T}=0.2$ corresponds to the charge ordering for $CO_{1/3}$. Sequential charge-ordering transition occurs from $CO_{1/3}$ to $CO_{1/4}$ around $\tilde{T}=0.015$ $[\equiv T_{CO}(\mathbf{q}_{1/4})]$, which is lower a little than the result in $\mathcal{H}_V$. Magnetic order at $\mathbf{q}_{1/3}$ appears around $\tilde{T}=0.1[\equiv T_N(\mathbf{q}_{1/3})]$. Below $T_{CO}(\mathbf{q}_{1/4})$, magnetic structure is also changed; the spin correlation functions at $\mathbf{q}_{1/4}$ and (5/12, 5/12, 0) become dominant. It is also

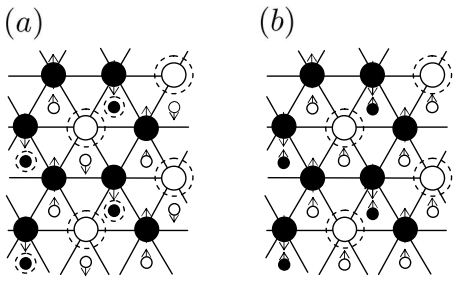

FIG. 13. Charge and spin structures in the polar $CO_{1/3}$ phase at $V_{cNNN}/V_{abNN}=0.6$. The filled and open circles represent Fe^{3+} and Fe^{2+}, respectively, and large and small circles are for Fe ions in the upper and lower planes, respectively. The arrows represent spin directions. At Fe sites surrounded by broken circles, spin directions are not uniquely determined. The spin structures in (a) and (b) are almost degenerate.

shown, in this parameter, that the electric polarization is enhanced in the $CO_{1/3}$ phase. A similar temperature dependence is obtained in $V_{abNN}/V_{cNNN}=0.61$, where the $CO_{1/2}-II$ phase appears in low temperatures instead of $CO_{1/4}$.

Low temperature charge and spin structures at $V_{cNNN}/V_{abNN}=0.6$ are shown in Fig. 13(a). Charge structure is identified to be $CO_{1/3}$. Spins at Fe^{3+} in the Fe^{2+}-$2Fe^{3+}$ (upper) plane and those at Fe^{2+} in the $2Fe^{2+}$-Fe^{3+} (lower) one are antiferromagnetically aligned. On the other hand, spin directions at Fe^{2+} in the Fe^{2+}-$2Fe^{3+}$ plane and at Fe^{3+} in the $2Fe^{2+}$-Fe^{3+} one are not uniquely determined. We note that the spin structure in the $2Fe^{2+}$-Fe^{3+} (lower) plane is sensitive to the parameter values in $\mathcal{H}_J$. The structures shown in Figs. 13(a) and 13(b) are almost degenerate with each other. The numerical results presented in this paper are obtained in the parameter sets where the spin structure in Fig. 13(a) is obtained. However, qualitative difference for the results in the two parameter sets is not seen. It is also true that the essence of the coupling between the spin ordering and the electric polarization shown in Fig. 11 does not depend on the detailed parameter values. Since the antiferromagnetic interaction between NN Fe^{3+}-Fe^{3+} bonds in the $2Fe^{3+}$-Fe^{2+} (upper) plane is robust, Fe^{2+} spins are surrounded by three up and three down spins in their NN Fe^{3+} sites. Therefore, spin directions in Fe^{2+} are not uniquely determined as explained above. Because the number of these sites is $N/3$, there is a macroscopic number of degenerate spin states of the order of $2^{N/3}$ which contributes to the entropy gain in finite temperatures. This is a kind of partially disordered phase, which has been examined in the antiferromagnetic Ising model on a triangular lattice.[46,47] In the present case, spins in Fe^{2+} and Fe^{3+} are inequivalent, i.e., $S=2$ and 5/2, and this partial disordered state becomes more stable in comparison to that in the conventional Ising model. Since this spin structure is realized in the $CO_{1/3}$ structure and the spin entropy is larger than the charge entropy in the nonpolar and partially polar charge-ordered phases, i.e., CO_A and CO_B, the polar $CO_{1/3}$ is reinforced through the spin-charge coupling in the exchange Hamiltonian. This is a kind of "order from fluctuation" mechanism, and, in the present spin-charge coupled system, a ferroelectric order is stabilized by spin fluctuation. This phenomenon is not expected in $CO_{1/2}-I$, $CO_{1/2}-II$, and

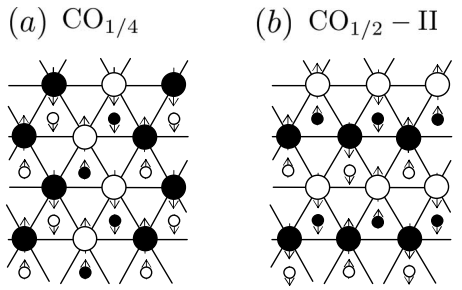

FIG. 14. (a) Charge and spin structure at $V_{cNNN}/V_{abNN}=0.59$ and that at 0.61 (b).

$CO_{1/4}$. Low temperature charge and spin structures in $V_{cNNN}/V_{abNN}=0.59$ and 0.61 are shown in Fig. 14. In both cases, all spins in NN Fe^{2+}-Fe^{2+} and Fe^{3+}-Fe^{3+} bonds are antiferromagnetically aligned. There are a number of degenerate spin states; for example, when all spins on a chain along [110] in $CO_{1/2}-II$ are flipped, the exchange energy is not changed. However, this spin degeneracy is of the order of $2^{\sqrt{N}}$, which is smaller than $O(2^{N/3})$ in $CO_{1/3}$.

In a remaining part of this section, we examine responses to the electric and magnetic fields in the present spin-charge coupled system. First, we pay our attention to the magnetic-field effect by introducing the Zeeman term of the Hamiltonian

$$\mathcal{H}_H = H\sum_i K_i^z, \tag{24}$$

where $K_i^z=I_i^z$ or J_i^z for Fe^{2+} or Fe^{3+}, respectively, and H is the magnetic field. The Hamiltonian $\mathcal{H}_V+\mathcal{H}_J+\mathcal{H}_H$ is analyzed by utilizing the MUMC method in a $6\times6\times2$-site cluster. Magnetic-field dependence of the electric polarization and the charge correlation functions at $V_{cNNN}/V_{abNN}=0.6$ and 0.59 are presented in Figs. 15 and 16, respectively. Temperature in the inset of Fig. 15(b) is chosen to be $\tilde{T}=0.05$, which is below the Néel temperature $T_N(\mathbf{q}_{1/3})$, and those in the inset of Fig. 16(b) are $\tilde{T}=0.05$ and 0.01, which are between $T_N(\mathbf{q}_{1/3})$ and the charge-ordering temperature of $CO_{1/4}$ $[T_{CO}(\mathbf{q}_{1/4})]$ and below $T_{CO}(\mathbf{q}_{1/4})$, respectively. When V_{abNN} is taken to be 1 eV, magnetic field $H/V_{abNN}=0.01$ corresponds to about 100 T. In the magnetically ordered $CO_{1/3}$ phases at $V_{cNNN}/V_{abNN}=0.6$ and 0.59, applying the magnetic field reduces the electric polarization. On the other hand, in the antiferromagnetic $CO_{1/4}$ phase at $V_{cNNN}/V_{abNN}=0.59$ [see $T<T_{CO}(\mathbf{q}_{1/4})$ in Fig. 16(b)], the electric polarization is induced by applying the magnetic field. At the same time, the charge correlation function $N(\mathbf{q}_{1/3})$ increases and $N(\mathbf{q}_{1/4})$ decreases. Similar results are obtained at $V_{cNNN}/V_{abNN}=0.61$, where the $CO_{1/2-II}$ phase collapses and the electric polarization appears below $\tilde{T}=0.015$ by applying the magnetic field. Thus, opposite magnetic-field effects are obtained in the magnetically ordered $CO_{1/3}$ phase and the antiferromagnetic $CO_{1/4}$ and $CO_{1/2-II}$.

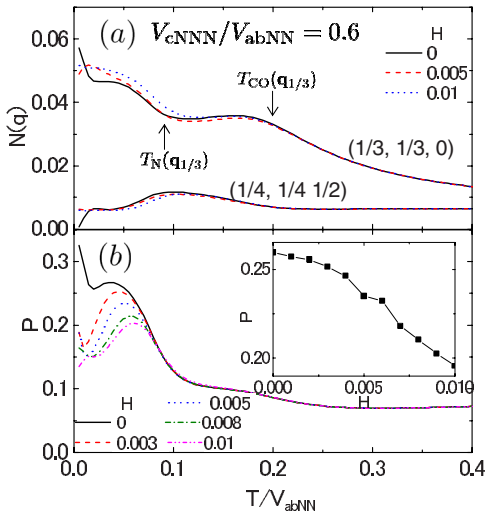

FIG. 15. (Color online) Magnetic-field effect in (a) charge correlation function $N(\mathbf{q})$ and (b) electric polarization P. The parameters are chosen to be $V_{cNN}/V_{abNN}=1.2$ and $V_{cNNN}/V_{abNN}=0.6$. The inset of (b) shows magnetic-field dependence of the electric polarization at $\tilde{T}=0.05$.

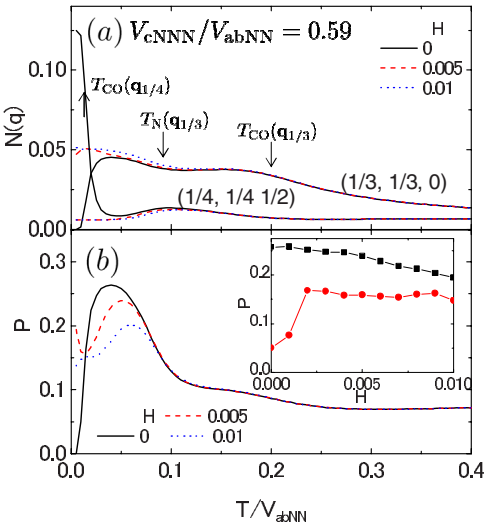

FIG. 16. (Color online) (a) Magnetic-field effect in charge correlation function $N(\mathbf{q})$ and (b) electric polarization P. Parameters are chosen to be $V_{cNN}/V_{abNN}=1.2$ and $V_{cNNN}/V_{abNN}=0.59$. The inset of (b) shows magnetic-field dependence of the electric polarization. The solid circles and squares are calculated at $\tilde{T}=0.01$ and 0.05, respectively.

We, first, pay our attention to the negative magnetic-field effect in the magnetically ordered $CO_{1/3}$ phase. As explained in Sec. III, the three charge structures, the polar $CO_{1/3}$, the partially polar CO_A, and the nonpolar CO_B, coexist at $H=0$. Among the three, the polar $CO_{1/3}$ is a dominant structure because of the large spin entropy due to the spin degeneracy of the order of $2^{N/3}$. By applying the magnetic field, these $N/3$ spins are aligned to be parallel to the magnetic field, and the macroscopic spin degeneracy is lifted. On the other hand, in both the nonpolar CO_B and the partially polar CO_A, a macroscopic degeneracy in the charge configuration, which is of order of $2^{\sqrt{N}}$, survives under the magnetic field. As the result, the charge entropy in CO_A and CO_B overcomes the spin one in $CO_{1/3}$, and P is reduced. In other words, under the magnetic field, the present spin-charge coupled system is

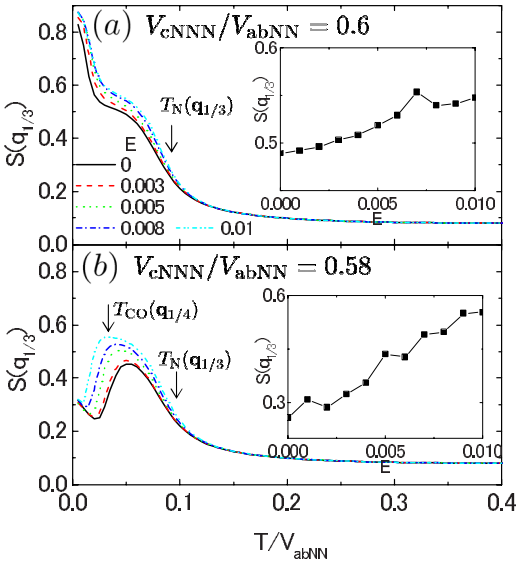

FIG. 17. (Color online) Electric-field effect of spin correlation function $S(\mathbf{q})$ at $\mathbf{q}_{1/3}$. The parameters are chosen to be (a) $V_{cNNN}/V_{abNN}=0.6$ and (b) 0.58 with $V_{cNN}/V_{abNN}=1.2$. The insets show electric-field dependence of $S(\mathbf{q}_{1/3})$. Temperatures are $\tilde{T}=0.05$ in (a) and 0.03 in (b).

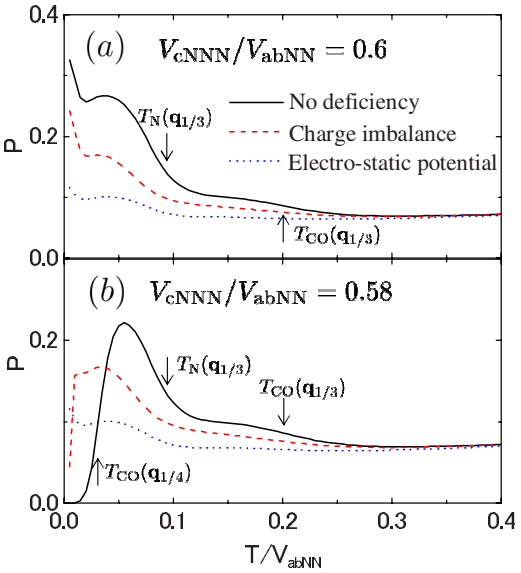

FIG. 18. (Color online) Oxygen-deficiency effects of electric polarization P at (a) $V_{cNNN}/V_{abNN}=0.6$ and (b) 0.58. The bold, broken, and dotted lines are for result without deficiency, with charge-imbalance effect and with electrostatic potential, respectively.

mapped onto a spinless model described by $\mathcal{H}_V$ where the charge entropy plays a dominant role. On the contrary, the positive magnetic-field effect in the antiferromagnetic $CO_{1/4}$ phase is explained from the Zeeman energy. Under the magnetic field, the ferrimagnetic structure in the polar $CO_{1/3}$ phase is more stable than the antiferromagnetic one in $CO_{1/4}$, and the polarization appears below $T_{CO}(\mathbf{q}_{1/4})$. However, under a high magnetic field larger than $H/V_{abNN}\sim 0.01$, the polar $CO_{1/3}$ competes with CO_A and CO_B, and the polarization decreases, as discussed above.

We are also able to demonstrate the response to the electric field in the present spin-charge coupled system. The static electric field E applied along the c axis is formulated by the Hamiltonian

$$\mathcal{H}_E = -eEd\sum_i^u Q_i^z, \tag{25}$$

where d is a distance between the two triangular-lattice planes in a W layer. Amplitude of the electric field $eEd/V_{abNN}=0.01$ corresponds to about 50 MV/m, when we take $V_{abNN}=1$ eV and $d=2.2$ Å. Electric-field dependences of the spin correlation functions at $V_{cNNN}/V_{abNN}=0.6$ and 0.58 are presented in Fig. 17. By applying the electric field, the spin correlation at $\mathbf{q}_{1/3}$ is enhanced, in particular, below $T_{CO}(\mathbf{q}_{1/4})$ in $V_{cNNN}/V_{abNN}=0.58$. This is a consequence of the polar $CO_{1/3}$ phase stabilized by the electric field. The results would be used as a test for the present scenario.

V. EFFECT OF OXYGEN DEFICIENCY

It is well known that several dielectric and magnetic properties in RFe_2O_4, e.g., charge and spin ordering temperatures, are extremely sensitive to the oxygen stoichiometry, which is denoted by δ in the formula $RFe_2O_{4-\delta}$.[33,35,48] Effects of the oxygen deficiency in this system are recognized as the impurity effects in charge-spin coupled system in a triangular lattice. Here, we examine roles of oxygen deficiency on the magnetoelectric phenomena. We simulate the following two aspects of the oxygen deficiencies: (1) charge imbalance between Fe^{2+} and Fe^{3+}, which is introduced by the modified charge conservation relation as $N^{-1}\Sigma_i Q_i^z=-2\delta$ and (2) random electrostatic potential around defect sites. This is modeled by the Hamiltonian

$$\mathcal{H}_R = 2\sum_i \sum_j{}' V_R(|i-j|)Q_j^z, \tag{26}$$

where Σ_i and Σ_j' represent summations of defect sites and that of the neighboring Fe sites, respectively. We assume that a defect site is in the FeO plane, and effective charge of a defect is 2+. Amplitudes of the electrostatic potentials are estimated by the $1/r$-type potential as $V_R=1.73V_{abNN}$ and $1.60V_{abNN}$ for the NN and next NN sites from a defect site, respectively. The model Hamiltonian $\mathcal{H}_V+\mathcal{H}_J+\mathcal{H}_R$ is analyzed with the relation $N^{-1}\Sigma_i Q_i^z=-2\delta$ by the MUMC method. One defect is introduced in a $6\times6\times2$-site cluster. This concentration corresponds to $\delta=0.05$.

In Fig. 18, oxygen-deficiency effect on the electric polarization is presented. In $CO_{1/3}$ [see below $T_{CO}(q_{1/3})$ in Fig. 18(a) and between $T_{CO}(\mathbf{q}_{1/3})$ and $T_{CO}(\mathbf{q}_{1/4})$ in Fig. 18(b)], both the charge-imbalance and electrostatic potential effects suppress the electric polarization. On the contrary, in the antiferromagnetic $CO_{1/4}$ phase below $T_N(\mathbf{q}_{1/4})$ in Fig. 18(b), the electric polarization is induced by both the two types of deficiency effects. These results are consistent with the electron-diffraction experiments in $YFe_2O_{4-\delta}$,[48] in samples with large δ, the fourfold-type charge order disappears, but

the threefold-type indexed as $(1/3\ 1/3\ 3m+1/2)$ is robust.

We turn to explain a mechanism of the charge-imbalance effect. Reduction in P in the $CO_{1/3}$ phase shown in Fig. 18(a) is a kind of a usual impurity effect which tends to break the long-range order. On the contrary, increase in P in low temperatures shown in Fig. 18(b) is related to the characteristic charge frustration in $CO_{1/3}$ as follows. The charge imbalance represented by a relation $N^{-1}\Sigma_i Q_i^z = -2\delta$ implies replacement of some Fe^{3+} ions in a stoichiometric system by Fe^{2+}. This corresponds to flipping of pseudospins Q_i^z. It is rather trivial, in Fig. 5, that this flipping of a Q_i^z uniquely happens in the $CO_{1/2}-I$, $CO_{1/2}-II$, and $CO_{1/4}$ structures. However, in $CO_{1/3}$, there are two ways to flip a Q_i^z because of the two-sublattice structure mentioned in Sec. III: Fe^{2+} sites surrounded by NN three Fe^{2+} and three Fe^{3+} in a plane (sublattice A) and those surrounded by six NN Fe^{3+} in a plane (sublattice B). A pseudospin in the sublattice A is able to be easily flipped in energy. We numerically calculate energy costs due to a flipping in sublattice A, which is about 40% of that in sublattice B, and is about 65% in $CO_{1/2}-II$ and $CO_{1/4}$. Such low-energy charge excitations in $CO_{1/3}$ stabilize the charge structure under the charge imbalance.

The electrostatic potential effect is also understood from a viewpoint of a soft charge structure in the $CO_{1/3}$ phase. Since an effective charge of a defect is 2+, Fe^{2+} ions, rather than Fe^{3+}, tend to assemble to screen this positive excess charge. However, due to the Coulombic interaction between Fe^{2+} ions, a simple cluster consisting of Fe^{2+} around a defect is not energetically favored. Exchange of Fe^{2+} and Fe^{3+} between the planes in a W layer is able to reduce such Coulombic energy. Energy cost for this kind of exchange of Fe^{2+} and Fe^{3+} is much lower in $CO_{1/3}$ than that in other charge-ordered structures. That is, the electrostatic screening for excess charge easily occurs in $CO_{1/3}$ because of the two-sublattice structure.

VI. DISCUSSION AND CONCLUDING REMARKS

Here, we have remarks on some issues that are not explicitly included in the present model and calculation. Effects of the electron transfer in $3d$ orbitals are not taken into account in Hamiltonian (18). This may be reasonable for the first-step theoretical model in RFe_2O_4. It is because, even above the three-dimensional charge-ordering temperature (250 K) in YFe_2O_4, the electric resistivity ρ shows an insulating behavior; ρ increases with decreasing temperature. A magnitude of ρ about 250 K is of the order of $10^2\ \Omega$ cm,[49] which is much larger that that above the Verwey transition in Fe_3O_4.[50] Therefore, we suppose that dominant electron motion is caused by thermal motion rather than quantum electron transfer. This is supported by the experimental data in the dielectric constant; it shows strong dispersive feature well described by the Debye model based on the thermal fluctuation of dipole moments.[23,30,51] Electron-transfer effects for the charge-ordered phase in a triangular lattice have been investigated for some low-dimensional organic salts.[52,53] In theoretical calculations based on the V-t and extended Hubbard models at quarter filling, a metallic phase appears in a parameter region between two different charge orders or it coexists with the threefold-type charge order. We suppose that small electron transfer in RFe_2O_4 stabilizes the $CO_{1/3}$ phase, although diffusive features in the dielectric function become more remarkable.

Lattice degree of freedom and a coupling with electron are not explicitly included in the present calculation. In our knowledge, there are no detailed crystal structure data in spin-charge-ordered phases. It is thought from the experimental analyses in YFe_2O_4 that the crystal symmetries in both the two- and three-dimensional charge-ordered phases indexed as $(1/3\ 1/3\ 3m+1/2)$ are trigonal, but that in the fourfold-type charge order is monoclinic.[48] This result indicates that the lattice distortion in the threefold-type charge order is weaker than that in other charge-ordered phases. This is consistent with the present results for a soft charge-order character in $CO_{1/3}$; amplitude of the charge correlation function is smaller than that in other phases. A weak lattice distortion expected in the threefold-type charge order is also related to the symmetry of the $CO_{1/3}$ structure, where the rhombohedral symmetry remains in a FeO planes, unlike other charge-ordered phases.

In Sec. IV, we show that the electric polarization is reinforced by the ferrimagnetic ordering, and this originates from the spin entropy in a triangular lattice. The long-range exchange interactions and/or the magnetostriction effects, which are not explicitly included in the present model, may release the spin degeneracy. In these cases, we suppose that the spins, which are not fixed in the present model [see Fig. 13], are loosely bounded by such low-energy scale interactions. However, these still fluctuate in a temperature region that is higher than the energy scale of the interactions and contribute to the entropy gain.

In the present paper, we analyze an electronic model defined in a single W layer that is recognized as a minimal and main stage in RFe_2O_4. Obtained results provide a starting point to elucidate a variety of magnetic and dielectric phenomena. We briefly discussed, in Sec. III, some roles of the inter-W-layer Coulomb interaction. To clarify the three-dimensional charge and spin structures[20,28,29,33] and the magnetodielectric response along the c axis, a more realistic modeling for the inter-W-layer interactions, in particular, the inter-W-layer exchange interactions, and analyses of a three-dimensional model are necessary.

In summary, electronic structure and magnetodielectric phenomena in the rare-earth iron oxides are examined. The model Hamiltonian describing the electronic interactions between charge, spin, and orbital degrees of freedom of Fe ions is derived. This model is analyzed by utilizing the Monte Carlo simulation in a finite size cluster. The threefold-type charge order associated with electric polarization is more stabilized in finite temperature than the nonpolar twofold- and fourfold-type charge orders. This originates from the two-sublattice structure in this polar phase; the Coulomb potential at a site in one of the sublattices from the in-plane NN sites is canceled out because of frustration. As a result, large charge fluctuation easily occurs and contributes to the entropy gain in finite temperature. It is shown that this polar phase is reinforced below the magnetic ordering temperature. The obtained threefold-type spin structure is consistent with the experimental results. This stabilization of the polar phase

is attributed to a macroscopic number of spin degeneracy caused by spin frustration. Because this spin structure occurs in the polar charge order, and the spin entropy surpasses the charge entropy in the nonpolar phases, the polar phase is stabilized through the spin-charge coupling in the exchange Hamiltonian. Magnetoelectric responses to the external fields are shown. By applying magnetic field in the threefold-type charge order, the electric polarization is reduced. This is interpreted that the spin degeneracy is quenched under the magnetic field. This result is available as a test of the present theory. We also study effects of the oxygen deficiency to which the dielectric and magnetic properties in $R\mathrm{Fe}_2\mathrm{O}_4$ are extremely sensitive. The threefold-type polar charge order is more robust than the twofold- and fourfold-type ones. This is attributed to the soft charge-order character in this polar phase; low-energy charge fluctuation reduces the energy cost by charge imbalance and electrostatic potential due to oxygen deficiency. Through the present study, we provide a unified picture for a variety of magnetic and dielectric phenomena in $R\mathrm{Fe}_2\mathrm{O}_4$.

ACKNOWLEDGMENTS

The authors would like to thank N. Ikeda, S. Mori, T. Arima, Y. Horibe, J. Akimitsu, K. Kakurai, N. A. Spaldin, M. Matsumoto, H. Matsueda, and J. Nasu for their valuable discussions. This work was supported by JSPS KAKENHI (Grant No. 16104005), TOKUTEI (Grant No. 18044001, 19052001, 19014003) from MEXT, NAREGI, and CREST.

APPENDIX A: EXCHANGE HAMILTONIAN

In this appendix, we show the details of the superexchange processes and an explicit form of the Hamiltonian $\mathcal{H}_J$ introduced in Sec. II. There are two kinds of the superexchange processes termed the *dd* and *dpd* processes as introduced in Eqs. (10) and (11). The Hamiltonian $\mathcal{H}_J$ is classified by valences of Fe ions, Fe^{m+}-Fe^{n+}, in the initial and final states, and the electronic structure in the intermediate states k [see Eq. (13)]. In this appendix, nearest neighboring Fe sites concerning in the superexchange interactions are denoted as i and j. Electron configurations in Fe and O ions are represented in a hole picture.

1. Exchange interactions in Fe^{2+}-Fe^{2+}

For the *dd* processes, electron configurations in the intermediate exchange processes are denoted as $d^3p^0d^5$. Five holes are at a site j and three holes at i with $S=3/2$. The intermediate states are classified by the spin and orbital states at site j [see Figs. 19(a)–19(c)]: (a) the total spin of Fe holes at site j, S is equal to 5/2 and both the two E' orbitals are occupied, (b) $S=3/2$ and the two E' are occupied, and (c) $S=3/2$ and one of the E' is occupied. The explicit forms of the exchange Hamiltonian are given by

$$\mathcal{H}^{(22)-1} = J^{(22)-1}\sum_{\langle ij\rangle} (\mathbf{I}_i \cdot \mathbf{I}_j + 6)(P_i^{\tau+}P_j^{\tau-} + P_i^{\tau-}P_j^{\tau+})P_i^{Q-}P_j^{Q-}, \tag{A1}$$

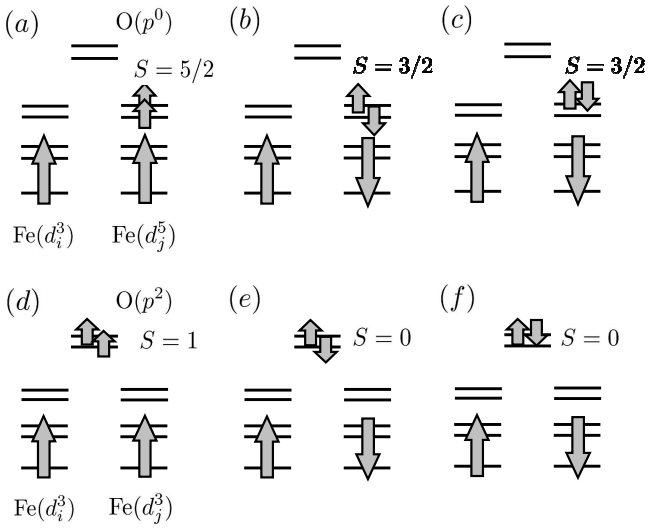

FIG. 19. Intermediate states of the exchange processes in a Fe^{2+}-Fe^{2+} bond represented by hole picture. (a)–(c) are for the Hamiltonian $\mathcal{H}^{(22)-1}$, $\mathcal{H}^{(22)-2}$, and $\mathcal{H}^{(22)-3}$ in the *dd* processes, respectively, and (d)–(f) are for $\mathcal{H}^{(22)-4}$, $\mathcal{H}^{(22)-5}$, and $\mathcal{H}^{(22)-6}$ in the *dpd* ones, respectively. Long and short arrows represent spins with $S=3/2$ and 1/2, respectively.

$$\mathcal{H}^{(22)-2} = J^{(22)-2}\sum_{\langle ij\rangle} (\mathbf{I}_i \cdot \mathbf{I}_j - 4)(P_i^{\tau+}P_j^{\tau-} + P_i^{\tau-}P_j^{\tau+})P_i^{Q-}P_j^{Q-}, \tag{A2}$$

$$\mathcal{H}^{(22)-3} = J^{(22)-3}\sum_{\langle ij\rangle} (\mathbf{I}_i \cdot \mathbf{I}_j - 4)P_i^{\tau+}P_j^{\tau+}P_i^{Q-}P_j^{Q-}. \tag{A3}$$

Here, we define the projection operators for charge

$$P_i^{Q\pm} = \frac{1}{2} \pm Q_i^z, \tag{A4}$$

and those for orbital,

$$P_i^{\tau\pm} = \frac{1}{2} \pm \tau_{i\eta_i}. \tag{A5}$$

The exchange parameters are given as $J^{(22)-1} = -t_{ddc}^2/[10\Delta_{(22)-1}]$, $J^{(22)-2} = t_{ddc}^2/[10\Delta_{(22)-2}]$, and $J^{(22)-3} = t_{ddc}^2/[4\Delta_{(22)-3}]$, and $\Delta_{(mn)-k}$ is the energy of the second order intermediate states given by $\Delta_{(22)-1} = W^d - I^d + \hat{V}$, $\Delta_{(22)-2} = W^d + 4I^d + \hat{V}$, and $\Delta_{(22)-3} = U^d + 4I^d + \hat{V}$. We define $t_{ddc} = t_{dd}^2 \cos\theta/\Delta_{\mathrm{CT}}$ and $t_{dds} = t_{dd}^2 \sin\theta/\Delta_{\mathrm{CT}}$.

In the intermediate states of the *dpd* process, two holes occupy the O ion. These states are classified by the spin and orbital states at the O site [see Figs. 19(d)–19(f)]: (d) the total spin of the O holes, S, is equal to 1 and both the p_x and p_y orbitals are occupied by holes, (e) $S=0$ and two p orbitals are occupied, and (f) $S=0$ and one of the p orbitals occupied by holes. The exchange Hamiltonians are given by

$$\mathcal{H}^{(22)-4} = J^{(22)-4}\sum_{\langle ij\rangle} (\mathbf{I}_i \cdot \mathbf{I}_j + 12)P_i^{\tau+}P_j^{\tau+}P_i^{Q-}P_j^{Q-}, \tag{A6}$$

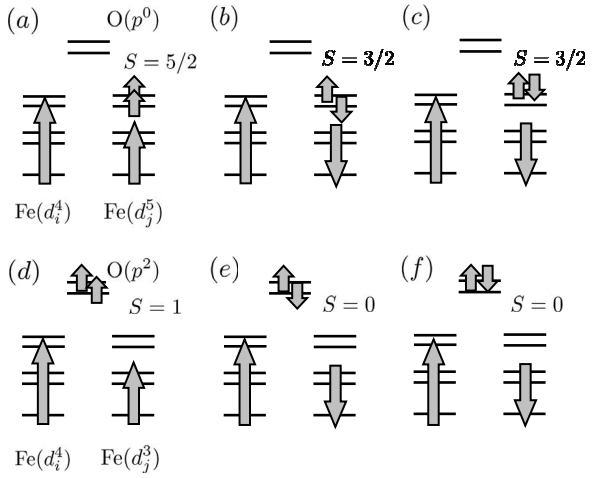

FIG. 20. Intermediate states of the exchange processes in a Fe^{2+}-Fe^{3+} bond represented by hole picture. (a)–(c) are for the Hamiltonian $\mathcal{H}^{(23)-1}$, $\mathcal{H}^{(23)-2}$, and $\mathcal{H}^{(23)-3}$ in the *dd* processes, respectively, and (d)–(f) are for $\mathcal{H}^{(23)-4}$, $\mathcal{H}^{(23)-5}$, and $\mathcal{H}^{(23)-6}$ in the *dpd* ones, respectively. Long, medium, and short arrows represent spins with $S=2$, 3/2, and 1/2, respectively.

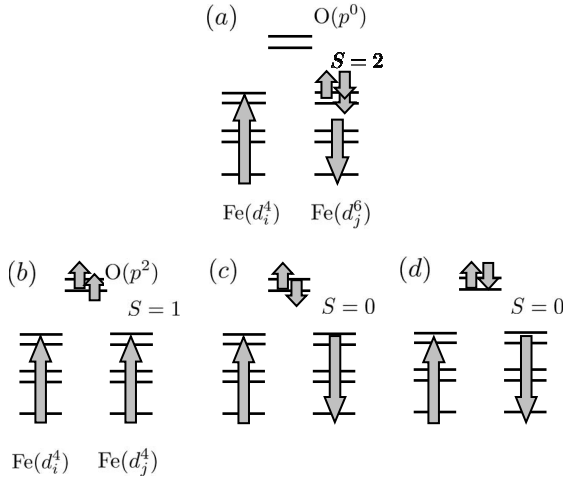

FIG. 21. Intermediate states of the exchange processes in a Fe^{3+}-Fe^{3+} bond represented by hole picture. (a) is for the Hamiltonian $\mathcal{H}^{(33)-1}$ in the *dd* processes, respectively, and (b)–(d) are for $\mathcal{H}^{(33)-2}$, $\mathcal{H}^{(33)-3}$, and $\mathcal{H}^{(33)-4}$ in the *dpd* ones, respectively. The long, medium, and short arrows represent spins with $S=2$, 3/2, and 1/2, respectively.

$$\mathcal{H}^{(22)-5} = J^{(22)-5}\sum_{\langle ij\rangle} (\mathbf{I}_i \cdot \mathbf{I}_j - 4) P_i^{\tau+} P_j^{\tau+} P_i^{Q-} P_j^{Q-}, \quad \text{(A7)}$$

$$\mathcal{H}^{(22)-6} = J^{(22)-6}\sum_{\langle ij\rangle} (\mathbf{I}_i \cdot \mathbf{I}_j - 4) P_i^{\tau+} P_j^{\tau+} P_i^{Q-} P_j^{Q-}. \quad \text{(A8)}$$

The exchange parameters are given as $J^{(22)-4} = -t_{dds}^2/[4\Delta_{(22)-4}]$, $J^{(22)-5} = t_{dds}^2/[4\Delta_{(22)-5}]$, and $J^{(22)-6} = t_{ddc}^2/[2\Delta_{(22)-6}]$, with $\Delta_{(22)-4} = 2\Delta_{\mathrm{CT}} + W^p - I^p$, $\Delta_{(22)-5} = 2\Delta_{\mathrm{CT}} + W^p + I^p$, and $\Delta_{(22)-6} = 2\Delta_{\mathrm{CT}} + U^p$.

2. Exchange interactions in Fe^{2+}-Fe^{3+}

Electron configurations in the intermediate states are $d^4p^0d^5$ and $d^4p^2d^3$ for the *dd* and *dpd* processes, respectively. As well as the exchange interaction in the Fe^{2+}-Fe^{2+} bond, these are classified by the spin and orbital structures in the d^5 and p^2 sites for the *dd* and *dpd* processes, respectively (see Fig. 20). The explicit forms of the exchange Hamiltonians are

$$\mathcal{H}^{(32)-1} = J^{(32)-1}\sum_{\langle ij\rangle} \left(\mathbf{J}_i \cdot \mathbf{I}_j + \frac{15}{2}\right) P_j^{\tau-} P_i^{Q+} P_j^{Q-}, \quad \text{(A9)}$$

$$\mathcal{H}^{(32)-2} = J^{(32)-2}\sum_{\langle ij\rangle} (\mathbf{J}_i \cdot \mathbf{I}_j - 5) P_j^{\tau-} P_i^{Q+} P_j^{Q-}, \quad \text{(A10)}$$

$$\mathcal{H}^{(32)-3} = J^{(32)-3}\sum_{\langle ij\rangle} (\mathbf{J}_i \cdot \mathbf{I}_j - 5) P_j^{\tau+} P_i^{Q+} P_j^{Q-} \quad \text{(A11)}$$

for the *dd* processes and

$$\mathcal{H}^{(32)-4} = J^{(32)-4}\sum_{\langle ij\rangle} (\mathbf{J}_i \cdot \mathbf{I}_j + 15) P_j^{\tau+} P_i^{Q+} P_j^{Q-}, \quad \text{(A12)}$$

$$\mathcal{H}^{(32)-5} = J^{(32)-5}\sum_{\langle ij\rangle} (\mathbf{J}_i \cdot \mathbf{I}_j - 5) P_j^{\tau+} P_i^{Q+} P_j^{Q-}, \quad \text{(A13)}$$

$$\mathcal{H}^{(32)-6} = J^{(32)-6}\sum_{\langle ij\rangle} (\mathbf{J}_i \cdot \mathbf{I}_j - 5) P_j^{\tau+} P_i^{Q+} P_j^{Q-} \quad \text{(A14)}$$

for the *dpd* ones. The exchange parameters are given as $J^{(32)-1} = -2t_{ddc}^2/[25\Delta_{(32)-1}]$, $J^{(32)-2} = 2t_{ddc}^2/[25\Delta_{(32)-2}]$, $J^{(32)-3} = t_{qdc}^2/[10\Delta_{(32)-3}]$, $J^{(32)-4} = -t_{dds}^2/[5\Delta_{(32)-4}]$, $J^{(32)-5} = t_{dds}^2/[5\Delta_{(32)-5}]$, and $J^{(32)-6} = 2t_{ddc}^2/[5\Delta_{(32)-6}]$, with $\Delta_{(32)-1} = \hat{V}$, $\Delta_{(32)-2} = 5I^d + \hat{V}$, $\Delta_{(32)-3} = U^d - W^d + 4I^d + \hat{V}$, $\Delta_{(32)-4} = 2\Delta_{\mathrm{CT}} + W^p - I^p$, $\Delta_{(32)-5} = 2\Delta_{\mathrm{CT}} + W^p + I^p$, and $\Delta_{(32)-6} = 2\Delta_{\mathrm{CT}} + U^p$.

3. Exchange interactions in Fe^{3+}-Fe^{3+}

Electron configurations in the intermediate states are $d^4p^0d^6$ and $d^4p^2d^4$ for the *dd* and *dpd* processes, respectively. In the d^6 configuration for the *dd* process, total spin is 2 [see Fig. 21(a)], and the explicit form is given by

$$\mathcal{H}^{(33)-1} = J^{(33)-1}\sum_{\langle ij\rangle} \left(\mathbf{J}_i \cdot \mathbf{J}_j - \frac{25}{4}\right) P_i^{Q+} P_j^{Q+}. \quad \text{(A15)}$$

The exchange parameter is $J^{(33)-1} = 4t_{ddc}^2/[25\Delta_{(33)-1}]$, with $\Delta_{(33)-1} = U^d + 4I^d + \hat{V}$. For the *dpd* processes, the intermediate states are classified by the spin and orbital structures in the O site [see Figs. 21(b)–21(d)]. The Hamiltonians are given by

$$\mathcal{H}^{(33)-2} = J^{(33)-2}\sum_{\langle ij\rangle} \left(\mathbf{J}_i \cdot \mathbf{J}_j + \frac{75}{4}\right) P_i^{Q+} P_j^{Q+}, \quad \text{(A16)}$$

$$\mathcal{H}^{(33)-3} = J^{(33)-3}\sum_{\langle ij\rangle} \left(\mathbf{J}_i \cdot \mathbf{J}_j - \frac{25}{4}\right) P_i^{Q+} P_j^{Q+}, \quad \text{(A17)}$$

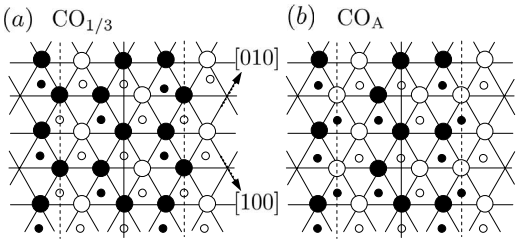

FIG. 22. (a) Schematic pictures of the $CO_{1/3}$ structure and (b) one of CO_A. When, in $CO_{1/3}$, Fe^{3+} in the upper plane and Fe^{2+} in lower one on chains indicated by the broken lines are exchanged, the CO_A structure in (b) is obtained.

$$\mathcal{H}^{(33)-4} = J^{(33)-4} \sum_{\langle ij \rangle} \left(\mathbf{J}_i \cdot \mathbf{J}_j - \frac{25}{4} \right) P_i^{Q+} P_j^{Q+}. \quad \text{(A18)}$$

The exchange parameters are $J^{(33)-2}=-4t_{dds}^2/[25\Delta_{(33)-2}]$, $J^{(33)-3}=4t_{dds}^2/[25\Delta_{(33)-3}]$, and $J^{(33)-4}=8t_{ddc}^2/[25\Delta_{(33)-4}]$, with $\Delta_{(33)-2}=2\Delta_{\mathrm{CT}}+W^p-I^p$, $\Delta_{(33)-3}=2\Delta_{\mathrm{CT}}+W^p+I^p$, and $\Delta_{(33)-4}=2\Delta_{\mathrm{CT}}+U^p$.

APPENDIX B: CHARGE STRUCTURES OF CO_A AND CO_B

In this appendix, detailed charge structures in the CO_A and CO_B phases, which are introduced in Sec. III, are presented. Charge configurations of CO_A are constructed from $CO_{1/3}$. Start from the $CO_{1/3}$ structure shown in Fig. 22(a), and focus on chains, e.g., along $[\bar{1}10]$, where different valences of Fe ions occupy the upper and lower planes. Let exchange all Fe^{2+} and Fe^{3+} in any of these chains with each other. One of the obtained configurations, termed CO_A, is shown in Fig. 22(b). These structures of CO_A are energetically degenerate with $CO_{1/3}$ in the Hamiltonian $\mathcal{H}_V+\mathcal{H}_J$. The Coulomb interaction between the second NN sites in the plane may lift the degeneracy. When the number the chains, where Fe^{2+} and Fe^{3+} ions are exchanged, is n $(0 \leq n < 2\sqrt{N}/3)$, the electric polarization is $P=N/3-n\sqrt{N}$. The degeneracy of a sum of these states is of the order of $\Sigma_{n2\sqrt{N}/3} C_n \sim 2^{\sqrt{N}}$. Such exchange of Fe ions is also allowed on chains along the [120] and [210] directions.

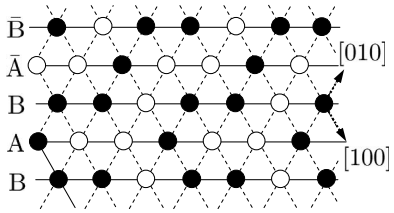

FIG. 23. One of the CO_B structures.

In another degenerated structure, CO_B, the configuration in one side of the W layer is constructed by stacking two kinds of chains alternately. These chains are schematically given as $\cdots\circ\circ\bullet\circ\circ\bullet\cdots$ (termed chain A) and $\cdots\bullet\bullet\circ\bullet\bullet\circ\cdots$ (chain B) along the [110] direction where $\bullet$ and $\circ$ represent Fe^{3+} and Fe^{2+}, respectively. As shown in Fig. 23, without energy loss of $V_{ab\mathrm{NN}}$, there are two ways to stack a chain A on a chain B, and vice versa. These are denoted as A and $\bar{A}$ and B and $\bar{B}$ in Fig. 23. Therefore, these configurations are degenerated of the order of $2^{\sqrt{N}}$. Charge configuration on another side of the W layer is uniquely determined to gain the interplane Coulomb interactions $V_{c\mathrm{NN}}$ and $V_{c\mathrm{NNN}}$. Obtained charge structures are degenerate with the $CO_{1/3}$ structure.

*Present address: Japan Medical Materials Co., Osaka 532-0003, Japan.

[1] T. Kimura, T. Goto, H. Shintani, K. Ishizaka, T. Arima, and Y. Tokura, Nature (London) **426**, 55 (2003).
[2] N. Hur, S. Park, P. A. Sharma, J. S. Ahn, S. Guha, and S.-W. Cheong, Nature (London) **429**, 392 (2004).
[3] K. Saitoh and K. Kohn, J. Phys.: Condens. Matter **7**, 478 (1995).
[4] S. W. Cheong and M. Mostvoy, Nat. Mater. **6**, 13 (2007).
[5] H. Katsura, N. Nagaosa, and A. V. Balatsky, Phys. Rev. Lett. **95**, 057205 (2005).
[6] M. Mostovoy, Phys. Rev. Lett. **96**, 067601 (2006).
[7] I. A. Sergienko and E. Dagotto, Phys. Rev. B **73**, 094434 (2006).
[8] M. Kenzelmann, A. B. Harris, S. Jonas, C. Broholm, J. Schefer, S. B. Kim, C. L. Zhang, S.-W. Cheong, O. P. Vajk, and J. W. Lynn, Phys. Rev. Lett. **95**, 087206 (2005).
[9] N. Aliouane, D. N. Argyriou, J. Strempfer, I. Zegkinoglou, S. Landsgesell, and M. v. Zimmermann, Phys. Rev. B **73**, 020102(R) (2006).
[10] Y. Yamasaki, H. Sagayama, T. Goto, M. Matsuura, K. Hirota, T. Arima, and Y. Tokura, Phys. Rev. Lett. **98**, 147204 (2007).
[11] E. J. W. Verwey, Nature (London) **144**, 327 (1939).
[12] See, a review, for example, M. Imada, A. Fujimori, and Y. Tokura, Rev. Mod. Phys. **70**, 1039 (1998).
[13] S. Maekawa, T. Tohyama, S. E. Barnes, S. Ishihara, W. Koshibae, and G. Khaliullin, *Physics of Transition Metal Oxides* (Springer-Verlag, Berlin, 2004).
[14] Y. Tokura, S. Koshihara, Y. Iwasa, H. Okamoto, T. Komatsu, T. Koda, N. Iwasawa, and G. Saito, Phys. Rev. Lett. **63**, 2405 (1989).
[15] M. H. Lemee-Cailleau, M. Le Cointe, H. Cailleau, T. Luty, F. Moussa, J. Roos, D. Brinkmann, B. Toudic, C. Ayache, and N. Karl, Phys. Rev. Lett. **79**, 1690 (1997).
[16] K. Yamamoto, S. Iwai, S. Boyko, A. Kashiwazaki, F. Hiramatsu, C. Okabe, N. Nishi, and K. Yakushi, J. Phys. Soc. Jpn. (to be published).
[17] Y. Tokunaga, T. Lottermoser, Y. Lee, R. Kumai, M. Uchida, T. Arima, and Y. Tokura, Nat. Mater. **5**, 937 (2006).
[18] D. V. Efremov, J. van den Brink, and D. I. Khomskii, Nat. Mater. **3**, 853 (2004).
[19] N. Kimizuka, E. Takayama-Muromachi, and K. Shiratori, in *Handbook on the Physics and Chemistry of Rare Earth*, edited by K. A. Gshneider, Jr. and L. Eyring (Elsevier, Amsterdam, 1990), Vol. 13, p. 283.
[20] Y. Yamada, K. Kitsuda, S. Nohdo, and N. Ikeda, Phys. Rev. B

62, 12167 (2000).
[21] Y. Yamada, S. Nohdo, and N. Ikeda, J. Phys. Soc. Jpn. **66**, 3733 (1997).
[22] Y. Zhang, H. X. Yang, C. Ma, H. F. Tian, and J. Q. Li, Phys. Rev. Lett. **98**, 247602 (2007); Y. Zhang, H. X. Yang, Y. Q. Guo, C. Ma, H. F. Tian, J. L. Luo, and J. Q. Li, Phys. Rev. B **76**, 184105 (2007).
[23] N. Ikeda, H. Ohsumi, K. Ohwada, K. Ishii, T. Inami, K. Kakurai, Y. Murakami, K. Yoshii, S. Mori, Y. Horibe, and H. Kito, Nature (London) **436**, 1136 (2005).
[24] J. Iida, Y. Nakagawa, and N. Kimizuka, J. Phys. Soc. Jpn. **55**, 1434 (1986).
[25] J. Akimitsu, Y. Inada, K. Shiratori, I. Shindo, and N. Kimizuka, Solid State Commun. **32**, 1065 (1979).
[26] K. Shiratori, S. Funahashi, J. Iida, and M. Tanaka, Proceedings of the Sixth International Conference of Ferrites (1992), p. 203.
[27] J. Iida, M. Tanaka, Y. Nakagawa, S. Funahashi, N. Kimizuka, and S. Takekawa, J. Phys. Soc. Jpn. **62**, 1723 (1993).
[28] A. D. Christianson, M. D. Lumsden, M. Angst, Z. Yamani, W. Tian, R. Jin, E. A. Payzant, S. E. Nagler, B. C. Sales, and D. Mandrus, Phys. Rev. Lett. **100**, 107601 (2008).
[29] K. Kakurai (private communication).
[30] N. Ikeda, K. Kohn, N. Myouga, E. Takahashi, H. Kito, and S. Takekawa, J. Phys. Soc. Jpn. **69**, 1526 (2000).
[31] N. Ikeda, K. Saito, and K. Kohn, Ferroelectrics **161**, 111 (1994).
[32] M. A. Subramanian, T. He, J. Chen, N. S. Rogado, T. G. Calvarese, and A. W. Sleight, Adv. Mater. (Weinheim, Ger.) **18**, 1737 (2006).
[33] S. Funahashi, J. Akimitsu, K. Shiratori, N. Kimizuka, M. Tanaka, and H. Fujishita, J. Phys. Soc. Jpn. **53**, 2688 (1984).
[34] N. Ikeda, R. Mori, K. Kohn, M. Mizumaki, and T. Akao, Ferroelectrics **272**, 309 (2002).
[35] N. Ikeda, R. Mori, S. Mori, and K. Kohn, Ferroelectrics **286**, 175 (2003).
[36] A. Nagano and S. Ishihara, J. Phys.: Condens. Matter **19**, 145263 (2007).
[37] A. Nagano, M. Naka, J. Nasu, and S. Ishihara, Phys. Rev. Lett. **99**, 217202 (2007).
[38] H. J. Xiang and M.-H. Whangbo, Phys. Rev. Lett. **98**, 246403 (2007).
[39] J. Nasu, A. Nagano M. Naka, and S. Ishihara, arXiv:0804.0843 (unpublished).
[40] B. Malaman, O. Evrard, N. Tannieres, A. Courtois and J. Protas, Acta Crystallogr., Sect. B: Struct. Crystallogr. Cryst. Chem. **31**, 1310 (1975).
[41] K. Kato, I. Kawada, N. Kimizuka, I. Shindo, and T. Katsura, Z. Kristallogr. **143**, 278 (1976).
[42] T. Mizokawa and A. Fujimori, Phys. Rev. B **54**, 5368 (1996).
[43] Y. Mizuno, T. Tohyama, S. Maekawa, T. Osafune, N. Motoyama, H. Eisaki, and S. Uchida, Phys. Rev. B **57**, 5326 (1998).
[44] B. A. Berg, J. Stat. Phys. **82**, 323 (1996).
[45] When the Fe^{2+} and Fe^{3+} ions are distinguished, this structure has the four sublattices. However, we call this, for simplicity, the two-sublattice structure.
[46] G. Wannier, Phys. Rev. **79**, 357 (1950).
[47] B. D. Metcalf, Phys. Lett. **46A**, 325 (1974).
[48] Y. Horibe, S. Shinohara, Y. Matsuo, S. Mori, K. Yoshii, and N. Ikeda (unpublished).
[49] M. Tanaka, J. Akimitsu, Y. Inada, N. Kimizuka, I. Shindo, and K. Shiratori, Solid State Commun. **44**, 687 (1982).
[50] Y. Kakudate, N. Mori, and Y. Kino, J. Magn. Magn. Mater. **12**, 22 (1979).
[51] N. Ikeda, K. Kohn, H. Kito, J. Akimitsu, and K. Siratori, J. Phys. Soc. Jpn. **63**, 4556 (1994).
[52] J. Merino, H. Seo, and M. Ogata, Phys. Rev. B **71**, 125111 (2005).
[53] C. Hotta and N. Furukawa, Phys. Rev. B **74**, 193107 (2006).